Bruno Miguel Rocha Martins
BsC

Electrochemical Supercapacitors Of Conductive Polymers And Their Composites

Dissertação Para Obtenção Do Grau De Mestre Em

Bioorgânica

Orientadora: M. Fátima Montemor, Prof. Dra., IST-UL

Co-orientadora: M. Margarida Cardoso, Prof. Dra., FCT-UNL

Júri:

Presidente: Prof. Doutora Paula Cristina de Sério Branco

Arguente: Prof. Doutora Raquel Alexandra Galamba Duarte

Vogal: Prof. Doutora Maria de Fátima Grilo da Costa Montemor

FACULDADE DE CIÊNCIAS E TECNOLOGIA
UNIVERSIDADE NOVA DE LISBOA

Setembro de 2014

PAGE INTENTIONALLY LEFT IN BLANK

Bruno Miguel Rocha Martins
BsC

Electrochemical Supercapacitors Of Conductive Polymers And Their Composites

Dissertação Para Obtenção Do Grau De Mestre Em

Bioorgânica

Orientadora: M. Fátima Montemor, Prof. Dra., IST-UL

Co-orientadora: M. Margarida Cardoso, Prof. Dra., FCT-UNL

Júri:

Presidente: Prof. Doutora Paula Cristina de Sério Branco

Arguente: Prof. Doutora Raquel Alexandra Galamba Duarte

Vogal: Prof. Doutora Maria de Fátima Grilo da Costa Montemor

FACULDADE DE CIÊNCIAS E TECNOLOGIA
UNIVERSIDADE NOVA DE LISBOA

Setembro de 2014

PAGE INTENTIONALLY LEFT IN BLANK

ELECTROCHEMICAL SUPERCAPACITORS OF CONDUCTIVE POLYMERS AND THEIR COMPOSITES

Copyright Disclaimer

ELECTROCHEMICAL SUPERCAPACITORS OF CONDUCTIVE POLYMERS AND THEIR COMPOSITES

Declaração de Direitos de Cópia

PAGE INTENTIONALLY LEFT IN BLANK

Acknowledgements

Regarding the work done on in this thesis I would like to acknowledge both my supervisors, Prof. M. Fátima Montemor and Prof. Margarida Cardoso for all the patience, support and the chance of doing this. I also want to acknowledge my family for their continual support and everybody in the GECEA group for all they have taught me.

Finally I would like to thank the coordinator of the Bioorganic Chemistry Masters in the New University of Lisbon (UNL) for the priceless chance and support she gave throughout my graduation.

PAGE INTENTIONALLY LEFT IN BLANK

Resumo

Neste trabalho experimental foram desenvolvidos supercondensadores de polianilina (PANI) suportada num substrato de aço inoxidável AISI304L e formada através de uma reação de auto-organização de polimerização por oxidação química em meio aquoso. O efeito de diversas variáveis na formação dos filmes e partículas depositadas, na sua morfologia e na capacidade específica destes, foi estudado. As variáveis estudadas foram: a espécie oxidante; as concentrações do oxidante, anilina, ácido sulfúrico e ácido fosfórico; e o efeito da adição de alguns óxidos metálicos. As melhores condições reaccionais, em relação às capacidades especificas electroquímicas foram: $4.15x10^{1}F.g^{-1}$, para $1x10^{-2}M$ de K_2S_2O8; $7.41x10^{1}F.g^{-1}$ para $1x10^{-2}M$ de anilina; $3.41x10^{2}F.g^{-1}$ para 5M de ácido fosfórico; $4.44x10^{2}F.g^{-1}$ para $5x10^{-1}M$ de ácido sulfúrico; $2.10x10^{2}F.g^{-1}$ para 34 horas de reação; e o melhor óxido metálico testado foi o dióxido de manganês (IV) com $1.60x10^{2}F.g^{-1}$.

Palavras-chave: polianilina, aço inoxidável AISI304L, supercondensadores, auto-organização

Abstract

In this experimental work, polyaniline (PANI) supercapacitors, supported on AISI304L stainless steel, were developed by self-assembly chemical oxidative polymerization in aqueous medium. The effect of several variables on the deposited films and particles, their morphologies and specific capacitances was studied. The variables studied were: oxidant species; oxidant, aniline, sulfuric acid and phosphoric acid concentrations; and effect of the addition of metallic oxides. The best reaction conditions, regarding the obtained specific capacitances were: $4.15x10^{1}F.g^{-1}$, for $1x10^{-2}M$ of K_2S_2O8; $7.41x10^{1}F.g^{-1}$ for $1x10^{-2}M$ of aniline; $3.41x10^{2}F.g^{-1}$ for 5M of phosphoric acid; $4.44x10^{2}F.g^{-1}$ for $5x10^{-1}M$ of sulphuric acid; $2.10x10^{2}F.g^{-1}$ for 34 hours of reaction; and the best metallic oxide tested was manganese (IV) dioxide with $1.60x10^{2}F.g^{-1}$.

Keywords: polyaniline, AISI304L stainless steel, supercapacitors, self-assembly

PAGE INTENTIONALLY LEFT IN BLANK

Table of Contents

Table of Figures

PAGE INTENTIONALLY LEFT IN BLANK

Table of Tables

Abbreviations List

μ - Charge mobility

σ – Electrical conductivity

BG – Band Gap

CB – Conduction Band

DMF - Dimethylformamide

DMSO - Dimethylsulfoxide

e – Electrical charge

EDLS - Electric Double Layer Supercapacitors

E_F – Fermi Energy Level Potential

EIS – Electrochemical Impedance Spectroscopy

ES – Electrochemical Supercapacitors

FS – Faradaic Supercapacitors

HOMO - Highest Occupied Molecular Orbital

K – Kelvin

LUMO - Lowest Unoccupied Molecular Orbital

n – Charge carriers density

NMP - 1-methyl-2-pyrrolidinone

PANI – Polyaniline

PEDOT - Poly(3,4-ethylenedioxythiophene)

PCA – Principal Component Analysis

Ppy - Polypyrrole

SCE – Saturated Calomel Electrode

T – Temperature

VB – Valence Band

PAGE INTENTIONALLY LEFT IN BLANK

1. Introduction

Environmental issues, fossil fuel availability and economical pressures have brought up urgency for clean, efficient and sustainable energy sources. With this, the need for new energy conversion and storage technologies also increases. From these, the ones which have attracted more attention in the last few years are fuel cells, batteries and electrochemical supercapacitors (ES)[1].

The source for the interest in ES is their high power density and output, and long lifecycle. They fill the gap between dielectric capacitors and batteries or fuel cells, which have high power output and high energy storage capacities. Despite the fact that the first supercapacitor patent was submitted in 1957, the real interest for this technology was only rekindled when the market of hybrid electric vehicles started to grow. This happened because ES are able to provide high power outputs, which are necessary for acceleration, and to accumulate some energy from the breaking process[1].

With the development of this ES technology other possible applications were found, such as power back-up elements for fuel cells and batteries when power disruptions occur, and voltage stabilizers. In fact, the US Department of Energy has declared ES as energy systems of the same importance of batteries and fuel-cells[1].

The current disadvantages of this technology are their high price compared to batteries and low energy density. The energy density is strongly dependent upon the electrode material given that it is the most important element in an ES[1]. Thus the search for cheaper and better performing materials for electrodes in electrochemical supercapacitors is crucial in order to achieve a broader range of possible applications and usage.

One of the main characteristics that is searched for in these materials is a high surface area and porosity. This arises from the fact that the energy can be stored at this interface between the electrode's electrically conductive material and the electrolyte. This can be treated like a conventional capacitor displaying an electrical double-layer according to the following expression:

$$C = \frac{A\varepsilon}{d}$$

where C is the capacitance, A is the active suface of the supercapacitor electrode, ε is the dielectric constant of the electrolyte and d is the thickness of the double layer. From this equation we can understand that the electrochemical supercapacitors are able to store large amounts of energy due to their large surface area and the short distance separating the charges at

its surface, when compared with conventional electrical double layer capacitors. Beyond these surface phenomena, certain electrode materials can themselves suffer electrochemical reactions.

These different phenomena are at the source of the main ES classes, namely, electric double layer supercapacitors (EDLS) and faradaic supercapacitors (FS). In EDLS the electrostatic energy is stored at the electrode/electrolyte interface in an electrode-potential-dependent way. At this interface, when a potential is applied, an accumulation or deficit of electric charges occurs at the surface of the electrode which is counterbalanced by charged electrolyte ions[1]. The most commonly used material for this type of supercapacitor is carbon (e.g. graphite oxide[2], carbon black[3], graphene[4], carbon nanotubes[5] and others[6]). In FS or pseudocapacitors the main charge storage mechanism is different. By applying a potential to these electrode materials a fast and reversible redox reaction occurs which causes a charge transfer between this and the electrolyte, a faradaic process. These redox reactions also cause electrostatic energy storage by electrolyte ions organization for charge counterbalancing (by electrosorption and ion intercalation) a non-faradaic process. Some of the types of materials which display this behaviour and have been studied for these applications are metallic oxides (e.g. MnO_2[7], Co_3O_4[8], $Ti_{0.6}Ru_{0.4}O_2$[9], NiO_x[10], $Ni(OH)_2$[11], V_2O_5[12], amongst others[13]) and conducting polymers (e.g. polyaniline (PANI)[14], polypyrrole (PPy)[15], poly(3,4-ethylenedioxythiophene) (PEDOT)[16], amongst others[17]).

2. Materials

In the last decades, the state of the art shows an increase in the creation of composites with materials that store energy by non-faradaic processes with those that do it with faradaic ones. Some examples of this are graphene/vanadium oxide nanotubes[18], graphene/PANI[19], Fe_3O_4/graphene[20], carbon nanotubes/polypyrrole[21], amongst others.

PANI was the material chosen for this study given that it is known having a high theoretical[22] electrochemical specific capacitance of 2000F.g^{-1}, low-cost monomer and an easy one-pot synthesis. ES electrodes of PANI[14] have reached values of 609F.g^{-1}, and PANI composites values of 1300F.g^{-1} with stainless steel[23] and 1486F.g^{-1} with carbon black[24].

2.1. Polyaniline as a Supercapacitor

Polyaniline was first discovered in 1835 as “aniline black”, a general expression used to refer to any product resulting from aniline oxidation[25]. It is one of the most studied conducting polymers given its environmental stability, easy synthesis (even in mild conditions), low cost of the monomer, and its useful and unique electrical, electrochemical and electrochromic properties[25-26]. These provide PANI with the potential to be used in various applications, such as: paints, antistatic textiles, sensors, capacitors, energy-storage devices, electromagnetic

shielding, non-linear optics, digital memory devices, artificial muscles, electrochromic displays, fuel cells, solar cells, diodes, organic or polymer light emitting diodes, p-n heterojunctions, amongst others[27]. However, despite all these and its easy processability, the fact that it decomposes at temperatures below those of softening or melting, makes its melt processing impossible[26].

The interest of PANI as a supercapacitor comes from the fact that the electrochemical redox processes that occur in its polymeric chains are basically a sequential production of Lewis bases that generate a multiply charged structure. The capacitance that arises from these is significant and can be regarded as redox pseudocapacitance. Given that these redox processes do not cause significant structural changes, and the metal-like behaviour of the polymer can formally describe this capacitance as being of the double-layer kind. In fact, the reversibility of these redox phenomena and the continuous range of oxidation potentials that occur with a growing applied pontential are behind the symmetrical cyclic voltammograms and the potential-sweep dependent response currents observed. Polyaniline can also be regarded as an organic semiconductor[28].

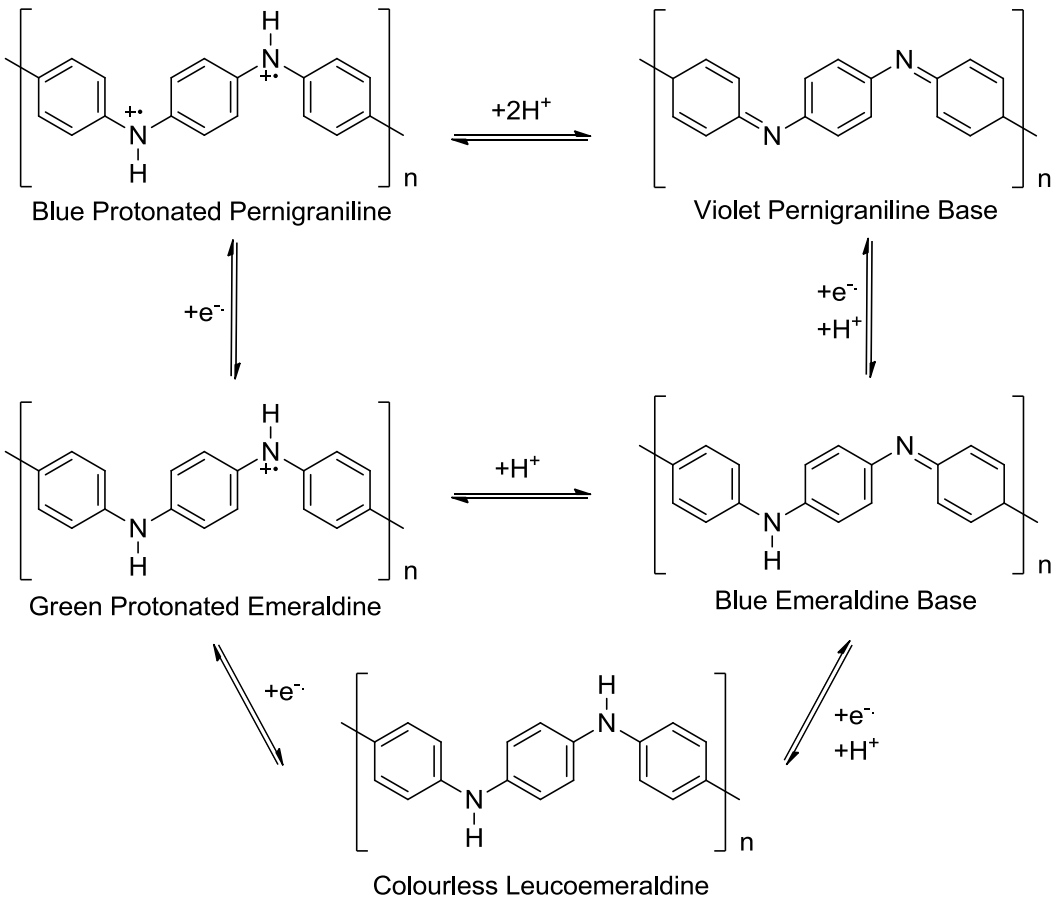

Figure 1 – Different polyaniline oxidation states and protonation levels[29].

Polyaniline can be synthesized by chemical, electrochemical, photochemical, sonochemical or plasma methods with or without template[27]. Chemical synthesis can be done by

oxidative polymerisation of aniline, either in organic or aqueous solvents, using oxidizing agents such as, $(NH_4)_2S_2O_8$[30], $FeCl_3$, KIO_3[26], NaClO, $K_2Cr_2O_7$[26], H_2O_2, enzymes, amongst others. The difficulties behind chemical synthesis are the impact of the following variables on its morphology and properties[26]: pH[31], aniline/oxidant ratio, cationic species present in solution[30], presence/absence of chiral species[32], reaction time and temperature[26], oxidizing agent species and concentration, and stirring speed[25]. Electrochemical deposition synthesis can be done by using, pulsed[33] or not, potentiostatic[26] or potentiodynamic/galvanostatic[26] methods.

After being synthesized some of PANI's properties can be altered by changing its morphology, oxidation state and/or pH. To change its morphology it can be either compressed[34] or dissolved, cast and then dried[26]. To dissolve it various aqueous or organic solvents can be used, amongst which concentrated acids (e.g. sulfuric acid, formic acid, acetic acid (80%)), dimethylformamide (DMF), dimethylsulfoxide (DMSO), 1-methyl-2-pyrrolidinone (NMP), amongst others[26]. The oxidation state can be easily changed by applying an external potential or using the adequate oxidant/reductant. pH, directly affects PANI's conductivity.

Another change that can be of interest is PANI's carbonisation to produce nitrogen-containing carbon materials which display distinct properties (e.g. catalytic properties, electrical conductivity, charge-storage ability, mechanical features) from undoped carbon materials[35].

2.2. Polyaniline Synthesis by Chemical Oxidation

There are various possible strategic approaches for synthesis of polyaniline by chemical oxidation synthesis, such as[27]: colloidal dispersion, emulsion, solution, interfacial, template-assisted, seeding, self-assembling and enzymatic polymerization.

In this work we will be using the self-assembling polymerization approach once it allows a deposition of PANI in surfaces of complex geometries without the need of applying an external energy source. It consists in placing a surface inside a solution where the oxidative polimerization is taking place and waiting for the formation of a film on its surface[27]. Once this is formed it is washed to remove any unreacted starting materials.

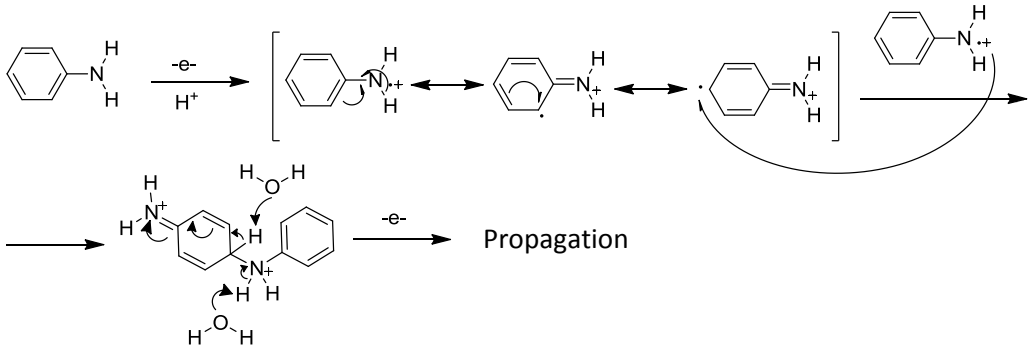

Figure 2 – Initiation mechanism of aniline chemical oxidative polymerization.

2.3. Electrical Conductivity in Polyaniline

Electrical conductivity (σ) is a phenomenon influenced by the density of charge carriers (n, in m^{-3}), their mobility (μ, in $m^2/(V.s)$) and carried charge (e, 1.6×10^{-19}C).

$$\sigma = en\mu$$

The type of charge carrier, its concentration and mobility can be determined by measuring the Hall effect. This also allows the determination of the type of semiconductor, p- or n-type, according to the signal of the Hall voltage. If it is negative the charge carriers are negative, a characteristic of n-type semiconductors, if it is positive, they are positive and the semiconductor of the p-type.

Literature describes PANI as a p-type semiconductor with "holes" as charge carriers[27]. In fact the "holes" are positive charges, which in practice should correspond to H^+ cations. The coalesced π orbitals form the valence band and the corresponding π^* orbitals form the conduction band. Thus the band-gap of the semiconducting PANI corresponds to the energy difference of the valence and the conduction bands. Polyaniline, like various other polymers, can have different levels of crystallinity depending on the chosen synthetic method[36,37] , a feature which has direct impact on its electrical conductivity. Semi-crystalline PANI is a heterogeneous system constituted by crystalline regions surrounded by other amorphous ones[27]. In the former the conduction is metallic-like, occurring through electron delocalization or charge carrier hopping through the polarons, which is possible in these areas with an ordered structure. The overall conductivity is thus affected by these metallic-like areas and the ease with which charge carriers are able to tunnel between the conducting and non-conducting phases.

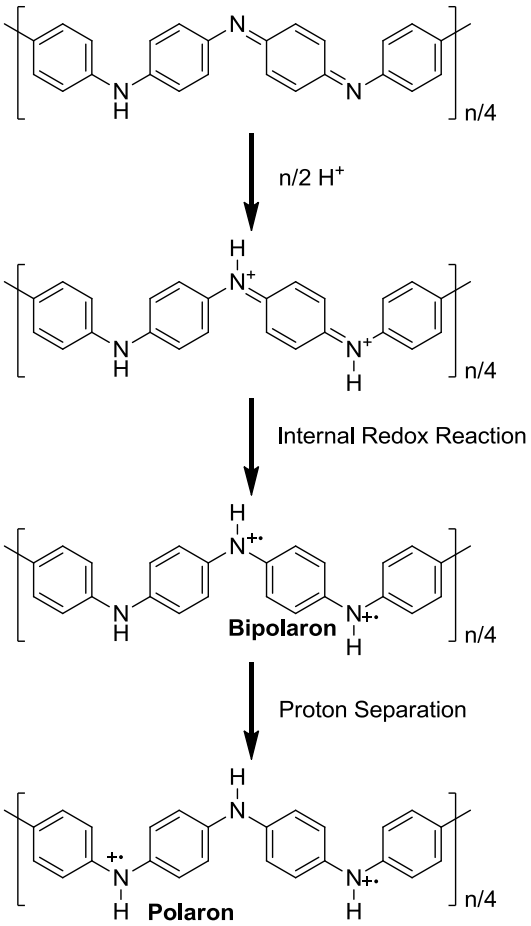

Figure 3 – From the top-down: emeraldine base before and after partial (50%) protonation, and corresponding bipolaron and polaron[27].

2.4. Semiconductors

Organic semiconductors are organic molecules or polymers with an extended conjugated π-electron system. Their ease of processing, ease of switching between isolating and conducting behavior (upon doping or change in oxidation state), and broad range of applications, make these very appealing materials for further development and production. Amongst their possible applications, the most common are: organic field effect transistors, organic light emitting diodes, organic electronics, energy storage and organic solar cells. Their properties can be easily tuned by adjusting the molecular structure, because this changes their highest occupied molecular orbital (HOMO) and lowest unoccupied molecular orbital (LUMO) energy levels. The tunability of these compounds makes them interesting for photocatalytic applications as well[38].

In solids, the energetic state structure has forbidden and allowed states for electrons (band gap and bands, respectively). The highest occupied energy band, in the ground state, is the valence band (VB), and the lowest unoccupied, the conduction band (CB). To the forbidden energy states between them we call band gap (BG)[38].

In direct band gap semiconductors, when an electron is excited it changes its energy, keeping its momentum. This allows the use of photon excitation and, consequently, UV/Vis or fluorescence to measure it. In indirect band gap semiconductors the energy and momentum of the electron change during excitation. To achieve this, the electron must interact with a lattice vibration and a photon (i.e. a phonon), a slow and unlikely process, when compared with the previous[38].

It is thus clear that a solid's band structure affects, such as its chemical composition and crystal structure, will affect its semiconducting properties. A well-studied example of this is TiO_2, which exists in three different structures: rutile, anastase and brookite. They all have the same basic building unit, a TiO_6 octahedron, but with different connection structures between them[38]. So the band gaps of these semiconductors are: 2.98eV for rutile, 3.05eV for anastase and 3.26eV for brookite[39].

So it is clear that the chemical structure alone is not enough to describe the semiconductor behaviour of a solid[38].

Once the electron-hole pair has been created, the semiconductor can act as a microelectrochemical cell. In this analogy the CB with the excited electron would act as the cathode and the hole at the VB as the anode[38].

The charge separation associated with the charge generation created by the electron excitation, and its lifetime is fundamental in understanding some of the properties of the semiconductor. The excited semiconductor can lose energy in various different ways, such as: recombination of the electron and hole; oxidation and reduction reactions; amongst others[38].

Impurities, crystal defects, crystallinaty, morphology and particle size of the semiconductor also affect the electron-hole pair recombination process, since they can act as or be a source of trapping areas. Thus crystals with an infinite periodic structure and no defects are the ideal target to achieve higher efficiencies. However, real crystals have crystal defects which allow for the analogy with an aggregate of ideal crystals. Knowing this, the smaller the crystal, the less defects it has, since it has less volume for different crystals. Despite this, the surface of the crystal also acts as a trapping area itself, so the surface to volume ratio is an important parameter to take into account when developing semiconductor nanocrystals. The crystal structure itself can increase charge separation and conduction by having a layered structure. It is proposed that this comes from the similarity between the nature of the layers and the VB and CB[38].

2.4.1. Doping

Metal-ion and nonmetal doping decreases the band-gap, by adding a trapping point to the structure or creating a mid-gap doping agent-induced level. Various non-metals were tested for doping agents, amongst which H, C, B, S and N. A wide range of techniques were used to do this, such as ion-implantation, sputtering, chemical vapor deposition and sol-gel. Various types of metals were used as doping agents: noble and/or transition metals and/or rare earth ions. Metallic addition to the semiconductor can have a band-gap reduction effect[38].

2.4.2. Properties of Organic Semiconductors

As described above the semiconductor properties of organic semiconductors arise from: π-electron delocalization over the σ-backbone; HOMO and LUMO energy levels, which correspond to the CB and VB, respectively; and the energy difference between them, the E_{BG}. The intermolecular bonds in organic semiconductors affect their crystallinity. This together with the bonding structure will affect the intermolecular π-π-interactions having a direct impact on the solid structure. The solid structure can thus be disordered, polycrystalline or even amorphous. Planar molecular structures with and adequate conjugated backbone (which allow a good π-π-stacking), and a good intermolecular π-delocalization will have a better electron delocalization and a narrower band gap[38].

When an organic solid electron is excited it moves from the VB into the CB generating an electron-hole pair. This pair has a small dielectric constant (usually between 0.5 to 1.0eV), is strongly bound, has a diffusion of only a few nanometers and is frequently localized on only one molecule given the low electronic wavefunction extension. Excitons like these are also known as Frenkel excitons. The electron-hole pair can recombine through various mechanisms, amongst which: photochemical catalytic reaction; interaction with electron acceptors or donors, such as chemical dopants; and interaction with chemical or physical defects (that are present in conjugated polymers with high density)[38].

3. Techniques

The main techniques used in this work were scanning electron microscopy (SEM) for morphology analysis, Raman microscopy for chemical structures analysis and electrochemical techniques such as cyclic voltammetry and charge/discharge cycles.

3.1. Scanning Electron Microscopy

Scanning electron microscopy is often used as a direct method for characterizing the porous structure of various structures, such as porous activated carbons. The advantage of this technique is the fact that it allows a direct view of the microstructure.

In this technique, the sample is irradiated by a finely focused electrom beam. The sample then generates different types of signals, such as: auger, secondary and backscattered electrons; photons; and X-rays. For SEM the signals with interest are the secondary and the backscattered electrons since these are influenced by the surface topography[40].

The porosity of a supercapacitor has a direct impact in its specific capacitance, since it affects its surface area and thus the size of the double-layer formed. According to IUPAC nomeclature micropores are those with less than 2nm in width, mesopores those between 2nm and 50nm and macropores above this value. In porous activated carbon substrates, this classification is closely related with the behaviour of molecules adsorbed in porous activated carbon. The micropores represent most of the surface available for adsorption, micropores are also involved in this, however to a smaller extent. Macropores act mainly as conduits to provide access to the smaller pores at the interior of the structure[41].

3.1.1. Raman Microscopy

Since the 1960's, Raman spectroscopy has been used in the identification of films, much like infrared spectroscopy. In fact in polymers it was also used for quantification studies, such as: co-monomer ratio and composition; pigment loading; and detection of other additives. Nowadays with the increases in the detectors sensitivity, laser stability and computer power, other uses have been established, such as: quality control, archaeology, forensic sciences and competitive analysis[42].

This spectroscopy is based on the Raman effect which results from the interaction of electromagnetic radiation with the vibrational and/or rotational movements of liquids or solids. This light/matter interaction can be analyzed as an energy-transfer mechanism. According to quantum mechanics, molecular motions are possible on allowed discrete energy states. Thus a change in these is associated with the loss or gain of energy quanta. So in an absorption process the molecule gains an energy quantum from light. In a spontaneous emission one or more quanta are lost as photons and the molecule's energy decreases in the same amount. If these processes involve two or more quanta at the same time, we are dealing with scattering. So if an energy quantum is annihilated (by absorption, for example) and simultaneously another is created (by emission, for example) we are in the presence of simple elastic scattering (which corresponds to the Rayleigh line in the spectrum). In these processes, the molecule is not changed. However if this process involves two quanta of different energy, which cause a change in the energy state of the molecule, we have an inelastic process, an example of which is the Raman scattering. Thus depending on the relative energy of the quanta created and the one annihilated we are in the presence of a Stokes or an anti-Stokes Raman scattering. If the

absorbed photon has a lower energy than the annihilated one, the emitted quanta is detected at a higher frequency, and thus we have an anti-Stokes Raman shift. In the opposite situation we have a Stokes Raman shift[43].

The main problem with these phenomena is their efficiencies, in relation to the incident light. Elastic scattering has a 10^{-3} efficiency and an inelastic one, 10^{-6}.[43]

By analysing differences on spectra from one polymer with several different morphologies, it was possible to conclude that this technique can also be used for determination of polymer crystallinity. Another useful application is the assessment of polymer chain orientation in relation to a fiber, in the case of a composite. This task becomes much simpler when the Raman spectrometer is coupled with a microscope, since it becomes easier to focus the laser beam on the desired location[42]. The main difficulty associated with the use of this technique for the above mentioned applications is the determination of adequate criteria. Some commonly used methods to find these are: analysing the ratio between the intensities or full-widths at half maximum of certain peaks of interest; principal component analysis (PCA); or other data mining techniques, such as artificial neural networks[42].

This technique however, is not without its difficulties. Most of these come from the fact that the operator can select various different variables: temperature, atmosphere composition, pressure, laser wavelength, laser intensity, exposure time, number of accumulations and detector grating (directly related with sensitivity). Sometimes even if the measurement is done with the same conditions, but in a different equipment some differences may arise from issues such as equipment calibration and laser centering. This makes it difficult to find absolute raman shift values for the same bond in study, in the literature. Another issue that must be taken into account is the possible effect that the laser can have on the sample. If it is too intense it can cause changes in the physical state of the sample, its crystallinity or even its chemical composition by promoting photochemical reactions[42 and 44]. The impact of all these variables on the peak wavenumber can go from a few cm^{-1} to as high as $16cm^{-1}$.[44]

This makes some of the models built to assess certain sample characteristics only applicable within the conditions in which the training data was obtained[42]. However in order to have reference values on which to base the composition analysis done with this technique, we present in the following table, the frequencies for the Raman peaks of the main materials present in our tested samples (whithin the analyzed frequency range 350-1650cm^{-1}).

Table 1 – Raman peak wavelengths taken from the literature[44, 45, 46 and 47], using different exposure times, accumulations and laser intensities from those used in this work. Legend: o.p. – out-of-plane; i.p. – in-plane; ~ - bond between single and double.

Wavenumber (cm^{-1})	Vibration	Reference
236.5	α-Fe_2O_3	44
243	α-FeOOH	44
245	γ-FeOOH	44
282.7	α-Fe_2O_3	44
295.2	α-Fe_2O_3	44
296	δ-FeOOH	44
298	Fe_3O_4	44
299	α-FeOOH	44
319	Fe_3O_4	44
350	γ-Fe_2O_3	44
373	γ-FeOOH	44
385	α-FeOOH	44
395.9	α-Fe_2O_3	44
400	δ-FeOOH	44
416	C-H wag (o.p.) and/or C-N-C torsion (o.p.) (Phenazine)	46
418	Fe_3O_4	44
452	O-Cr^{III}-O	47
479	α-FeOOH	44
492.3	α-Fe_2O_3	44
493	γ-FeOOH	44
500	γ-Fe_2O_3	44
522	γ-FeOOH	44
550	α-FeOOH, Fe_3O_4	44
558	O-Cr^{III}-O	47
576	Phenoxazine-like segment; Benzenoid ring	46
596	α-Fe_2O_3	44
609	C-S stretch; SO_2 bending (i. p.)	46
630	O-Cr^{III}-O	47
632	C-S stretch; SO_2 bending (i. p.); Amine deformation (i. p.); Benzenoid ring deformation (i. p.)	46
650	γ-FeOOH	44
676	Fe_3O_4	44
680	δ-FeOOH	44
685	α-FeOOH	44
700	γ-Fe_2O_3	44
719	γ-FeOOH	44
728	C-C ring deformation	46
807	C-H (o. p.) deformation (quinonoid ring); C-H wag (o.p); ring deformation (semiquinonoid)	46
823	O-Cr^{III}-O	47
879	C-N-C wag (o.p.); Benzenoid ring deformation	46
889	Cr^{VI}-O	47
900-1100	P-O stretch	45

981	Cr^{VI}-O	47
993	α-FeOOH	44
1120	α-FeOOH	44
1153	O-H band deformation (CrOOH)	47
1160	δ-FeOOH	44
1169	C-H stretch (semiquinonoid ring)	46
1179	O-H band deformation (CrOOH)	47
1232	C-N stretch (benzenoid ring)	46
1255	α-FeOOH	44
1260	C-N stretch (benzenoid ring)	46
1303	γ-FeOOH	44
1314	δ-FeOOH	44
1322	Fe_3O_4	44
1337	$C\sim N^+$ stretch (Phenazine; Safranine-like segment; Phenoxazine-like segment)	46
1368	$C\sim N^+$ stretch (Safranine-like segment)	46
1404	Phenazine; Safranine-like segment; Phenoxazine-like segment	46
1513	N-H wag	46
1537	water H-O-H bending	46
1570	C~C (o.p.) (quinonoid ring and/or Phenazine)	46
1593	water H-O-H bending	46
1594	C=C wag (quinonoid ring); C~C wag (semi-quinonoid ring)	46
1624	C~C wag (benzenoid ring)	46
1634	water H-O-H bending	46
1640	Phenazine; Safranine-like segment; Phenoxazine-like segment	46

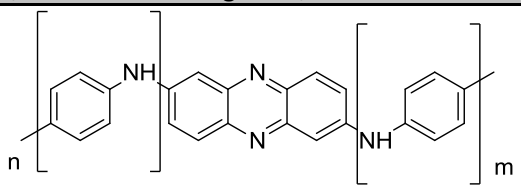

Phenazine-like segment

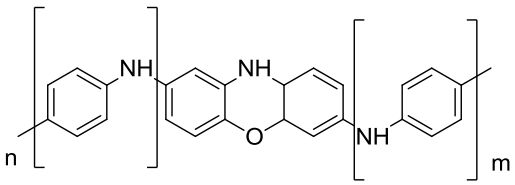

Phenoxazine-like segment

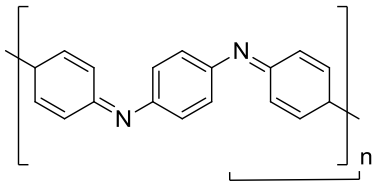

Quinonoid segment

Figure 4 – Examples of different structures usually detected by Raman spectra of PANI synthesized by chemical oxidative polymerization in aqueous medium.

4. Materials and Methods

The reagents used were: aniline and sulfuric acid (H_2SO_4) 96% from Sigma-Aldrich, potassium persulfate ($K_2S_2O_8$) and phosphoric acid (H_3PO_4) 85% from Fluka, manganese (IV) dioxide (MnO_2) from May&Baker and zinc oxide (ZnO) from the British Drug Houses Limited. All the water used was milipore and the aniline freshly vacuum distilled with zinc chloride ($ZnCl_2$)[48] from Sigma-Aldrich.

The carbon substrates used (see table bellow) were from Kynol Europa GmbH, and the AISI304L stainless steel from Goodfellow.

Table 2 – Activated carbon substrates used.

Activated Carbon Substrate	Weight /g.m^{-2}	Specific Surface Area /m^2.g^{-1}
Carbon Fabric (ACC-507-15)	120	1500
Carbon Felt (ACN-157-15)	90	1500
Carbon Felt (ACN-211-15)	180	1500

Table 3 – AISI304L stainless steel composition

AISI304L	C /%	Si /%	Mn /%	P /%	S /%	Cr /%	Ni /%	N /%
Minimum	-	-	-	-	-	18.00	8.00	-
Maximum	0.03	1.00	2.00	0.045	0.03	20.00	12.00	0.10

To study the effect of different variables on the chemical deposition of PANI, eight different reaction sets were done. In each of them one variable was changed, however the stirring speed of 600rpm and the reaction temperature of 23ºC was maintained for all reactions. Given the number of reactions, unless otherwise indicated in the tables below, their starting composition will be of 0.1M Aniline, 0.05M H_2SO_4, 0.05M H_3PO_4 and 0.05M $K_2S_2O_8$; their substrate an AISI304L stainless steel plate polished with a 500 grit SiC paper from Buehler; and 24 hours reaction time. This will hereafter be referred to as the reference reaction conditions.

Table 4 – Reaction set 1 tested variable: substrate effect.

Set	Variable Tested	Substrate	Substrate Pre-treatment
1	Substrate Effect	Carbon Fabric (ACC-507-15)	-
		Carbon Felt (ACN-157-15)	-
		Carbon Felt(ACN-211-15)	-
		AISI304L Stainless Steel	Ethanol degreasing + polishing with 500 grit SiC paper
			Ethanol degreasing + polishing with 1000 grit SiC paper
			Ethanol degreasing + polishing with 4000 grit SiC paper

Table 5 - Reaction set 2 tested variable: oxidant species effect.

Set	Variable Tested	Oxidant Species
2	Oxidant	$FeCl_3$
		NaClO
		$K_2S_2O_8$
		$NaNO_3$
		H_2O_2

Table 6 - Reaction set 3 tested variable: oxidant ($K_2S_2O_8$) concentration.

Set	Variable Tested	$[K_2S_2O_8]$ /M
3	Oxidant ($K_2S_2O_8$) Concentration	$1x10^{-3}$
		$1x10^{-2}$
		$5x10^{-2}$
		$1x10^{-1}$
		$2x10^{-1}$
		1

Table 7 - Reaction set 4 tested variable: aniline concentration.

Set	Variable Tested	[Aniline] /M
4	Aniline Concentration	$1x10^{-3}$
		$1x10^{-2}$
		$1x10^{-1}$
		1
		$1x10^{1}$

Table 8 - Reaction set 5 tested variable: H_3PO_4 concentration.

Set	Variable Tested	[H_3PO_4] /M
5	H_3PO_4 Concentration	$5x10^{-4}$
		$5x10^{-3}$
		$5x10^{-2}$
		$5x10^{-1}$
		5

Table 9 - Reaction set 6 tested variable: H_2SO_4 concentration.

Set	Variable Tested	[H_2SO_4] /M
6	H_2SO_4 Concentration	$5x10^{-4}$
		$5x10^{-3}$
		$5x10^{-2}$
		$5x10^{-1}$
		5

Table 10 - Reaction set 7 tested variable: reaction time.

Set	Variable Tested	Time /h
7	Reaction time	2
		4
		16
		24
		38
		48

Table 11 - Reaction set 8 tested variable: metallic oxide particle addition.

Set	Variable Tested	Species	Concentration /M
8	Metallic Oxide Particle Addition	-	-
		ZnO	$1x10^{-1}$
		MnO_2	

The deposited masses were determined by mass difference, using a Sartorius MC5 scale.

The composition of the films deposited over the substrates was determined by Raman Microscopy using an Horiba LabRAM HR Evolution with a Horiba LabSpec v6.01.1 software. The Raman spectra were done using a 532nm laser with 2mW of intensity for 20 accumulations of 30 seconds each.

Figure 5 - Horiba LabRAM HR Evolution (adapted from ref. [49])

The deposits morphology and thickness were analyzed by Scanning Electron Microscopy (SEM) using a Hitachi equipment operated at 20KeV.

To determine the specific capacitance of the electrodes, electrochemical techniques were used: cyclic voltammetry and galvanostatic charge-discharge cycling. These measurements were carried out using a VoltaLab PZ100 Potentiostat/Galvanostat in a three electrode cell. The working electrode was the sample in test, the counter electrode a Pt wire kept at a constant 2cm distance from the work electrode and a saturated calomel electrode (SCE) as reference electrode. For this reason, unless indicated otherwise, all the potentials mentioned throughout this work will be with respect to a SCE electrode. The cyclic voltammetry measurements were done at 50mV.s^{-1} potential sweep rate. The charge/discharge cycles were done by applying a 10A.g^{-1} current to the samples whithin their capacitive potential range.

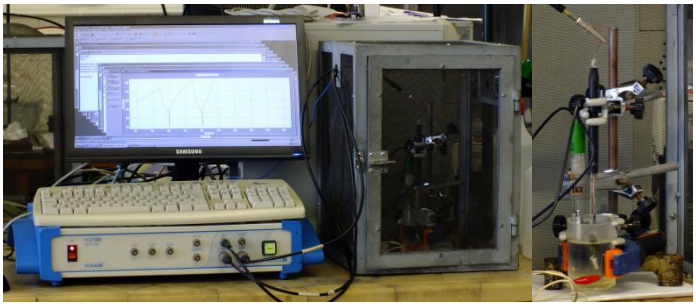

Figure 6 – Experimental setup used in electrochemical tests (left) and detail of the electrochemical cell (right).

The specific capacitance was calculated from the discharge step of the charge/discharge curve using the following equation[22],

$$C_s = \frac{i \times \Delta t_{discharge}}{m \times \Delta E}$$

where C_s is the electrochemical specific capacitance, i the current applied, m the mass of the electrode and ΔE the potential range used.

Surface resistivity measurements were done using a two-electrode multimeter.

5. Results and Discussion

The morphology of PANI structures is affected by a wide range of variables, and because of this so will its electrochemical specific capacitance[14]. Currently no systematic study on the impact of different variables on the capacitive performance of self-assembled PANI on AISI304L stainless steel is available on the scientific literature. So this study was developed to approach that issue.

As mentioned in the introduction there are various variables that can affect the morphology of PANI structures. In this study the following variables were tested: oxidant

species, oxidant concentration, pH, anionic species concentration, aniline concentration, reaction time and addition of metallic oxides.

The study started by a substrate screening to try and select the most adequate for PANI self-assembly and simultaneously a supercapacitor application. This is hereafter referred to as reaction set 1.

5.1. Reaction Set 1 – Substrate Effect

In this reaction set, substrates of different surface hydrophilicity were tested: hydrophilic, AISI304L stainless steel; and hydrophobic carbon felt and both carbon.

Stainless steel has a polar surface because of the presence of metallic oxides, mainly iron, chromium and nickel which should have affinity with the amine side of the aniline molecule as well as with the anilinium cations.

Carbon fabrics and felt are mainly composed of graphitic structures which will show a higher affinity for the apolar side of the aniline molecule and for PANI oligomers which are mainly apolar.

Each of these substrates was immersed in a reaction flask where the reference reaction was occuring for twenty four hours. PANI was formed/adsorbed over all of the tested surfaces. The deposited masses are shown in the table below.

Table 12 – Mass and conductivity of the PANI self-assembled over the substrates tested.

Set	Variable Tested	Substrate	Substrate Pre-treatment	PANI mass /mg	Surface Resistivity /Ω
1	Substrate Effect	Carbon Fabric (ACC-507-15)	-	22.19	200
		Carbon Felt (ACN-157-15)	-	3.01	1200
		Carbon Felt (ACN-211-15)	-	1.55	100
			Ethanol degreasing + polishing with 500 grit SiC paper	0.12	1.7
			Ethanol degreasing + polishing with 1000 grit SiC paper	0.27	2.8
			Ethanol degreasing + polishing with 4000 grit SiC paper	0.24	8.0

Despite having cut all samples to the same area, all of them had different specific surface areas. However no surface area measurements were done, making it impossible to ascertain the mass of PANI deposited per unit of specific surface area. In fact even if these were determined by physisorption techniques, the probe molecules usually used on these are H_2 or N_2 which occupy different areas than aniline, thus giving an inaccurate value of the surface available to our monomer. Thus, all the results are normalized to the mass of deposited PANI.

Despite the fact that the substrate with the highest deposited mass is a carbon fabric, the goal of this work is the development of PANI supercapacitors, so the main criterion used in the selection of the substrate was the electrical resistivity of the surface. This attribute was chosen since the aim is to develop supercapacitors having as little internal resistance as possible, allowing for faster charge transfer process. Thus the samples of AISI304L stainless were the selected ones. From these, the most conductive was the substrate polished with the SiC paper, 500 grit. Hence, this was the substrate chosen for subsequent reaction sets.

5.2. Reaction Set 2 – Oxidant Species

Various of the published studies about PANI were done using ammonium persulfate or iron(III) chloride as oxidant species. In the present work it was decided to use potassium persulfate instead of ammonium persulfate as the oxidant in the reference reaction. This choice was taken given the fact that potassium ion has a higher ionic mobility than the ammonium cation. This is of importance for the fact that PANI is considered a p-type organic semiconductor, thus having positive species as charge carriers. However it was still necessary to test other oxidizing agents, such as $FeCl_3$, NaClO, H_2O_2 and $NaNO_3$. All of these species have higher oxidation potentials than those of aniline. The results are presented in the following table.

Table 13 – Mass of self-assembled deposit over the AISI304L stainless steel substrate per unit of sample area.

Set	Variable Tested	Oxidant Species	Deposited Mass/Sample Area /g.cm^{-2}
2	Oxidant	$FeCl_3$	Below detection limit
		NaClO	$9.17x10^{-6}$
		$NaNO_3$	No deposit
		H_2O_2	Below detection limit
		$K_2S_2O_8$	$1.74x10^{-5}$

As can be seen the only samples in which we had a measurable deposit were those with NaClO and $K_2S_2O_8$ as oxidant species. Between these, the one with the highest deposit was the later with 47% more deposited mass.

The chemical composition of the deposited coating was analyzed by Raman microscopy. The corresponding spectra are shown in the figure below.

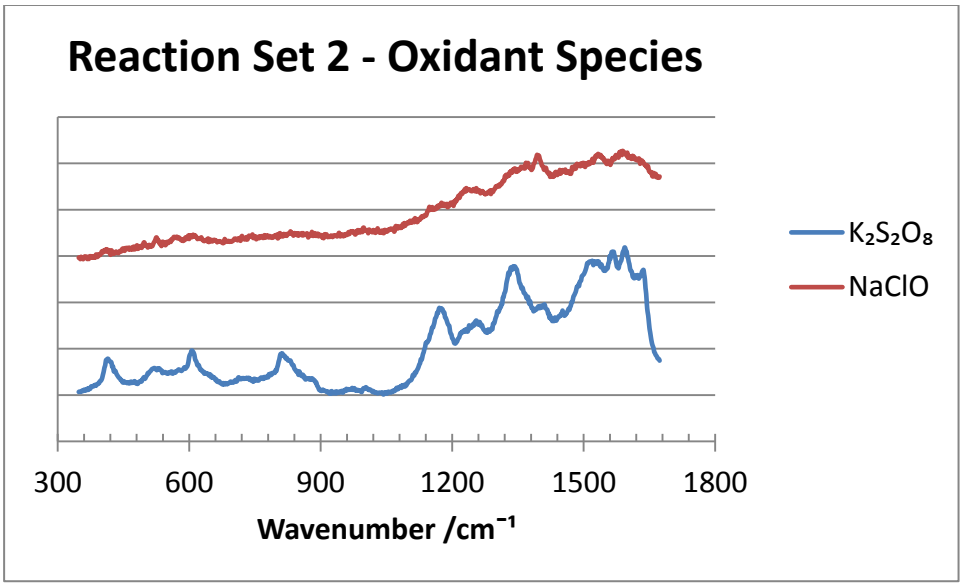

Figure 7 – Raman spectra of the surface of the AISI304L stainless steel samples exposed to the reactions of set 2.

There are significant differences between the two spectra. The main difference between them is that in the spectrum of the reaction done with NaClO the number of peaks from the stainless steel substrate is much higher. This may indicate that the compound formed at the surface had a higher affinity for specific metal oxides. The Raman peaks from metal oxides are: 398cm^{-1} (α-Fe_2O_3), 481cm^{-1} (α-FeOOH), 525cm^{-1} (γ-FeOOH), 565cm^{-1} (O-Cr^{III}-O), 602cm^{-1} (α-Fe_2O_3), 1175cm^{-1} (O-H band deformation from CrOOH) and 1248cm^{-1} (α-FeOOH). In the spectrum from the reaction with $K_2S_2O_8$, we can only see the following peaks from the substrate: 506cm^{-1} (γ-Fe_2O_3), 521cm^{-1} (γ-FeOOH) and 702cm^{-1} (γ-Fe_2O_3).

In both spectra water was detected (1593cm^{-1}), however only in the reaction with the persulfate did we detect peaks from the expected PANI counter-ions, phosphate (954 and 978cm^{-1} from P-O stretch) and sulfate (607cm^{-1} from SO_2 bend).

Regarding aniline and its reaction products, from the reaction done with NaClO the following peaks are visible: 1232cm^{-1} (C-N stretch (benzenoid ring)); 1342cm^{-1} (C~N+ stretch (phenazine, safranine-like segment, and/or phenoxazine-like segment)); 1369cm^{-1} (C~N+ stretch (safranine-like segment)); 1397 and 1446cm^{-1} (phenazine; safranine-like segment; phenoxazine-like segment); 1485cm^{-1} (N-H wag); 1573cm^{-1} (C~C (o.p.) (quinonoid ring and/or phenazine)); and 1626cm^{-1} (C~C wag (benzenoid ring)).

From the reaction with $K_2S_2O_8$: 414cm^{-1} (C-H wag (o.p.) and/or C-N-C torsion (o.p.) (phenazine)); 809 and 812cm^{-1} (C-H (o. p.) deformation (quinonoid ring), C-H wag (o.p), and/or ring deformation (semiquinonoid)); 1232cm^{-1} (C-N stretch (benzenoid ring)); 1340cm^{-1} (C~N+ stretch (phenazine, safranine-like segment, and/or phenoxazine-like segment)); 1397 and

1424cm^{-1} (phenazine, safranine-like segment and/or phenoxazine-like segment); 1508 and 1519cm^{-1} (N-H wag); 1564cm^{-1} (C~C (o.p.) (quinonoid ring and/or phenazine)); and 1623cm^{-1} (C~C wag (benzenoid ring)).

From these peaks alone one cannot say with certainty if the species correspond to aniline oligomers or polymer, and in this last case, which oxidation state it is in. So to be able to differentiate between these, photos taken with the Raman microscope were used.

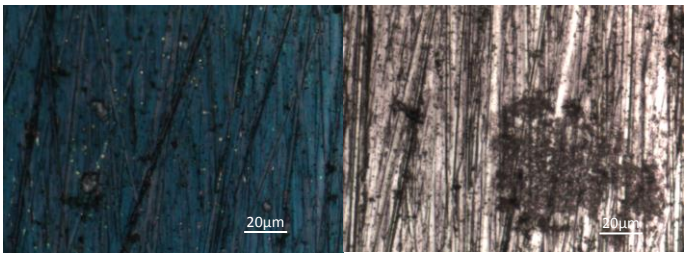

Figure 8 – Photos taken with the Raman microscope (50x magnification) of the surface of the samples from the reactions with $K_2S_2O_8$ (left) and NaClO (right).

From these photos it is possible to observe that the reaction done with potassium persulfate formed a film of PANI polymer in the emeraldine base state (blue color), whereas the one with sodium hypochloride seems to have formed some agglomerations of PANI oligomers (amorphous and brown).

Electrochemical measurements were made to assess the specific capacitance of these structures. Figure 10 shows the five cycles of the voltammetric curve.

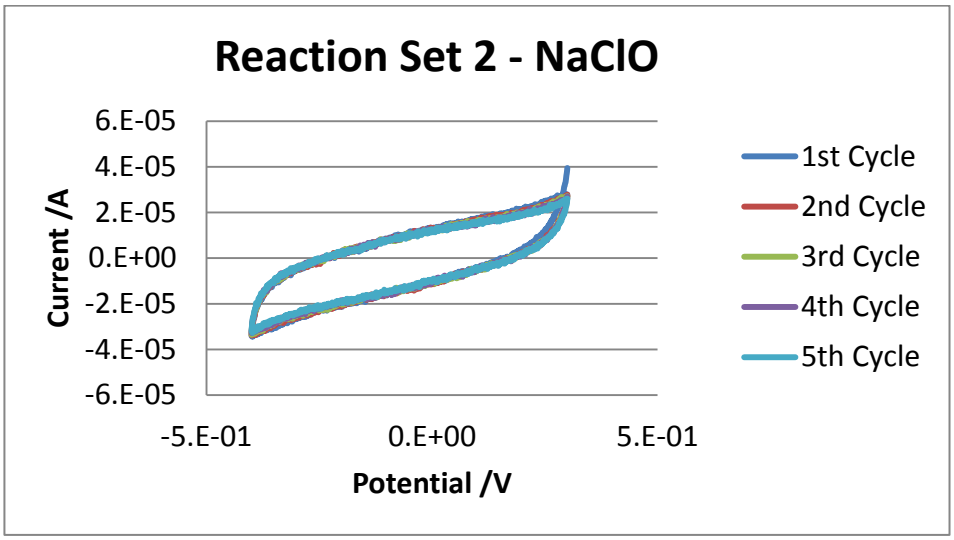

Figure 9 – Cyclic voltammogram of sample from reaction set 1 done using NaClO as the oxidant species. The potential range is between -400 and 300mV, electrolyte H_3PO_4 solution at pH 2 and potential sweep speed of 50mV.s^{-1}.

To find the potential window in which the samples displayed capacitive behaviour cyclic voltammetry was made in H_3PO_4 solution at pH 2. Other three electrolytes were tested,

HNO_3 (at pH 2), H_2SO_4 (at pH 2) and KOH (at pH 14), however they all had a damaging effect on the system. They either dissolved the polymer and/or reacted with it. Another reason for the choice of this electrolyte, both for electrochemical studies and the synthetic procedure itself is the known impact of the phosphate group in the conductivity of PANI[37].

The capacitive potential range was considered found when it was possible to overlap sucessive cyclic voltammograms in the widest potential range. This criterion was chosen given that it is a consequence of purely reversible phenomena. Various potential sweep speeds were tested, however no obvious oxidation and reduction peaks from PANI were found. This phenomenon has already been described in the literature for PEDOT, another conducting polymer, as being evidence of electrolyte ion orientation as the only phenomenon occurring in that potential window[50].

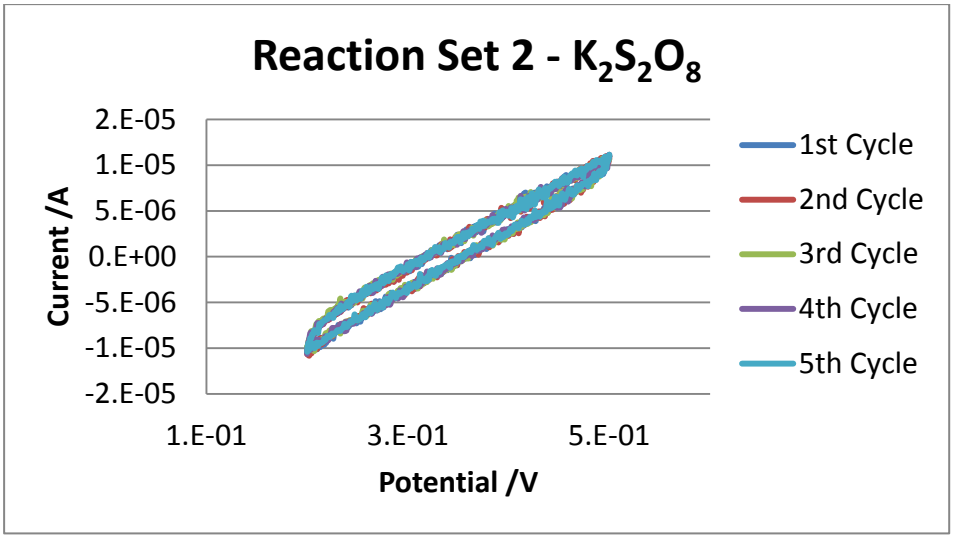

Figure 10 - Cyclic voltammogram of sample from reaction set 1 done using $K_2S_2O_8$ as the oxidant species. The potential range is between 200-500mV, electrolyte H_3PO_4 solution at pH 2 and potential sweep speed of 50mV.s^{-1}.

Thus the potential windows selected for the samples prepared with NaClO and $K_2S_2O_8$ were -400 to 300mV and 200-500mV, respectively. The cyclic voltammogram of the PANI synthesized with $K_2S_2O_8$, is very thin and tilted, which is characteristic of highly resistive materials. Thus we expect to have a very small value of electrochemical specific capacitance from this electrode. Within these potential windows charge/discharge cycles were done by applying a current of 10A.g^{-1}.

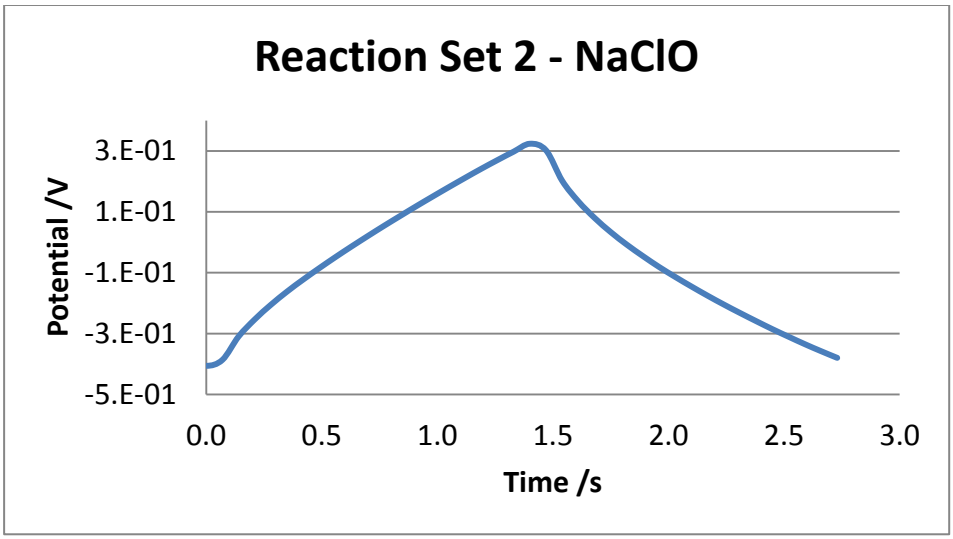

Figure 11 – Charge-discharge cycle of sample from set 1 with NaClO using 10A.g^{-1} current. The potential range is between -400 and 300mV and the electrolyte H_3PO_4 solution at pH 2.

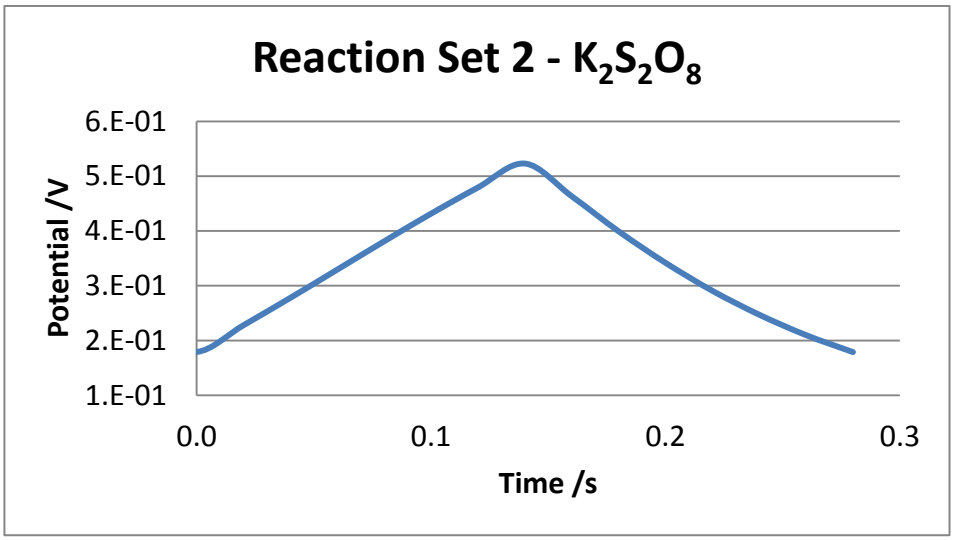

Figure 12 - Charge-discharge cycle of sample from set 1 with $K_2S_2O_8$ using 10A.g^{-1} current. The potential range range is between 200 and 500mV and the electrolyte H_3PO_4 solution at pH 2.

So the specific capacitance, at 10A.g^{-1}, of the sample done using NaClO is of 39.26F.g^{-1} and that with $K_2S_2O_8$, is 1.94x10^{-3}F.g^{-1}. Despite the electrode prepared using NaClO as oxidant having a higher specific capacitance value, its surface was very heterogeneously covered and the deposited mass was smaller. Thus the chosen oxidant species for the following reaction sets was $K_2S_2O_8$.

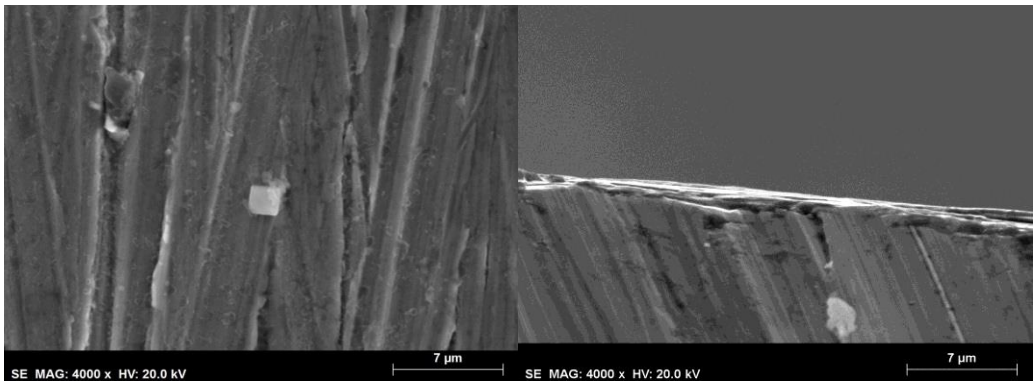

Figure 13 - SEM of the top (left) and cross-section (right) of the sample of reaction set 2 done using NaClO.

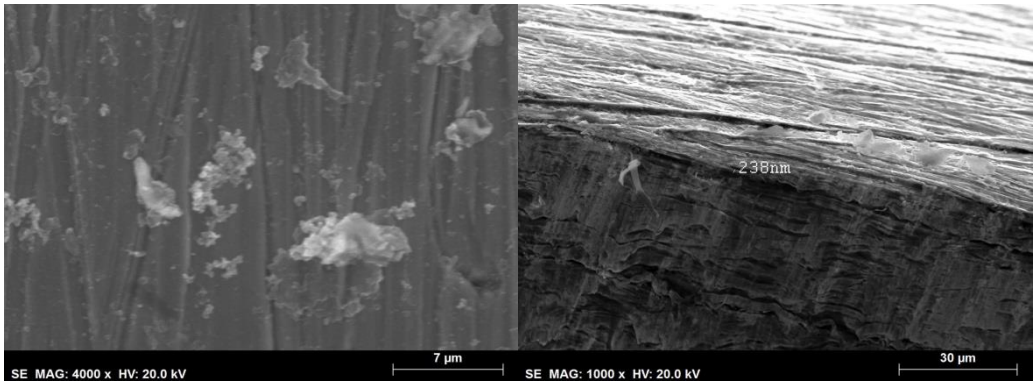

Figure 14 - SEM of the top (left) and cross-section (right) of the sample of reaction set 2 done using $K_2S_2O_8$.

By analysing the SEM images it is possible to confirm the absence of a uniform coating in the reaction done using NaClO and the existence of one with 238nm using $K_2S_2O_8$.

5.3. Reaction Set 3 – Oxidant Concentration

Once the oxidant species was chosen, the effect of its concentration was studied. As can be seen in the following table, the highest mass deposit is obtained with a $1x10^{-1}$M of oxidant.

Table 14 - Mass of deposit self-assembled over the AISI304L stainless steel substrate per unit of sample area.

Set	Variable Tested	$[K_2S_2O_8]$ /M	Deposited Mass/Sample Area /g.cm^{-2}
3	Oxidant ($K_2S_2O_8$) Concentration	$1x10^{-3}$	Below detection limit
		$1x10^{-2}$	$4.72x10^{-6}$
		$5x10^{-2}$	$1.74x10^{-5}$
		$1x10^{-1}$	$3.98x10^{-5}$
		$2x10^{-1}$	$2.60x10^{-5}$
		1	Below detection limit

The composition of the coating formed on the surface of each sample was analyzed by Raman microscopy revealing very similar spectra. The main differences are in the relative intensity and slight shifts in the wavelength of some peaks.

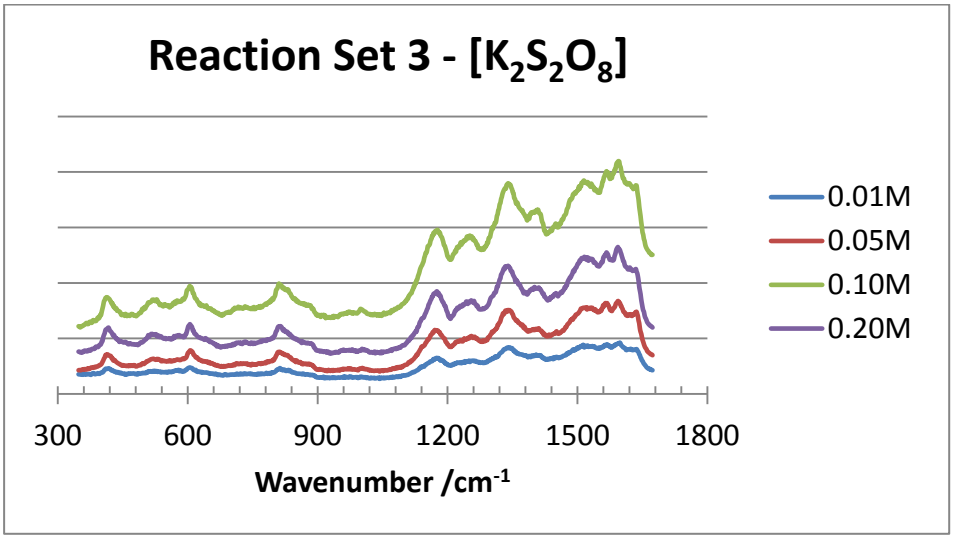

Figure 15 - Raman spectra of the surface of the AISI304L stainless steel samples exposed to the reactions of set 3.

In all these Raman spectra it is possible to observe peaks which indicate the formation of aniline oligomers and/or polymers. Namely at 414cm^{-1} for 1x10^{-2}M and 2x10^{-1}M and at 417cm^{-1} for 5x10^{-2}M and 1x10^{-1}M, which correspond to the phenazine's C-H and/or C-N-C out-of-plane wag and torsion, respectively. Other related peaks are visible at 1338cm^{-1} for 1x10^{-2}M and 1340cm^{-1} for 5x10^{-2}M, 1x10^{-1}M and 2x10^{-1}M, for the C~N^{+} stretch on phenazine or safranine-like segments; and at 1623cm^{-1} for 1x10^{-2}M and 5x10^{-2}M, and 1621cm^{-1} for 1x10^{-1}M 2x10^{-1}M, for the C~C wag of the benzenoid ring.

The Raman spectra also confirms the presence of sulfate ions by their visible peaks at 605cm^{-1} for 1x10^{-2}M, 1x10^{-1}M and 2x10^{-1}M and 607cm^{-1} for 5x10^{-2}M. All spectra show the phosphate P-O stretch vibrations in the 900-1000cm^{-1} region.

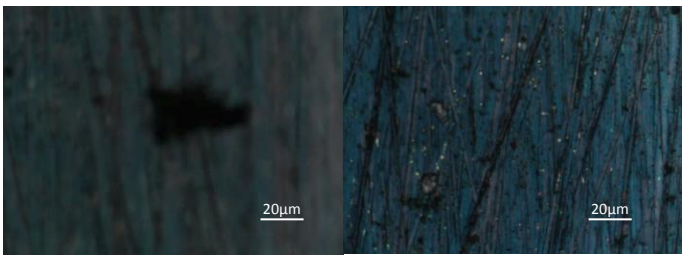

Figure 16 - Photos taken with the Raman microscope (50x magnification) of the surface of the samples from the reactions with 1x10^{-2}M (left) and 5x10^{-2}M of $K_2S_2O_8$.

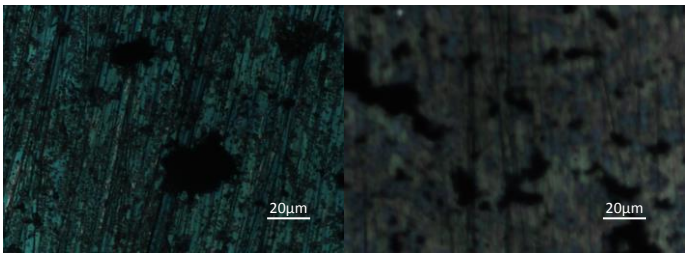

Figure 17 - Photos taken with the Raman microscope (50x magnification) of the surface of the samples from the reactions with $1x10^{-1}$M (left) and $2x10^{-1}$M of $K_2S_2O_8$.

From the photos taken of the surface of the samples it is possible to observe that all the reactions which yielded a measurable mass, namely those made with $1x10^{-2}$M, $5x10^{-2}$M, $1x10^{-1}$M and $2x10^{-1}$M of $K_2S_2O_8$ formed a film of PANI polymer in the emeraldine base state (blue color).

Electrochemical charaterization of the samples was done, revealing the following specific capacitances and potential ranges with capacitive behaviour.

Table 15 – Potential intervals and specific capacitances of the deposits formed on the surface of the AISI304L stainless steel samples exposed to the reactions of set 3.

$[K_2S_2O_8]$ /M	Film Thickness /nm	Potential Window /V	Specific Capacitance /F.g^{-1}
$1x10^{-2}$	1560	-0.40 to 0.20	$4.15x10^{1}$
$5x10^{-2}$	238	-0.30 to 0.15	$1.94x10^{-3}$
$1x10^{-1}$	743	-0.35 to 0.25	5.40
$2x10^{-1}$	821	-0.43 to 0.30	$1.59x10^{1}$

Thus, the potassium persulfate concentration which yields the best performing capacitor is $1x10^{-2}$M.

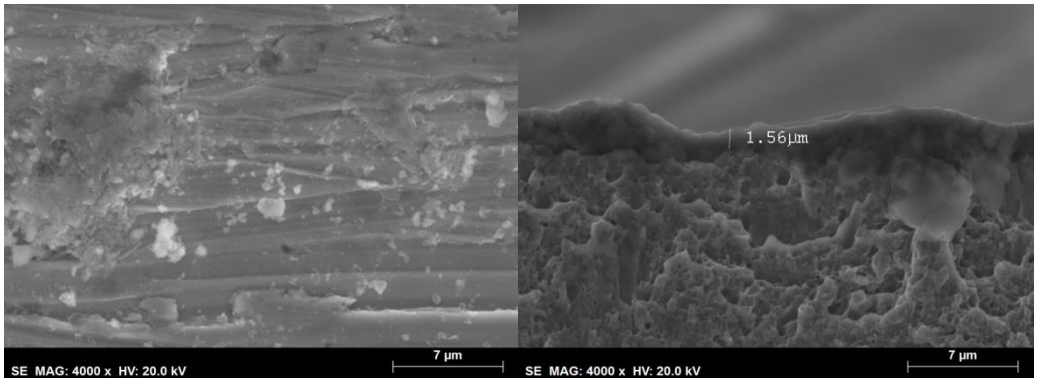

Figure 18 – SEM of the top (left) and cross-section (right) of the sample of reaction set 3 done using $1x10^{-2}$M of $K_2S_2O_8$.

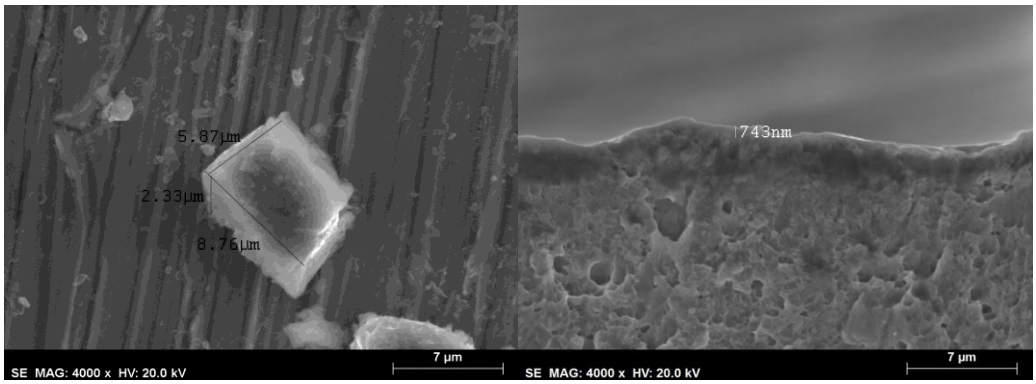

Figure 19 - SEM of the top (left) and cross-section (right) of the sample of reaction set 3 done using $1x10^{-1}$M of $K_2S_2O_8$.

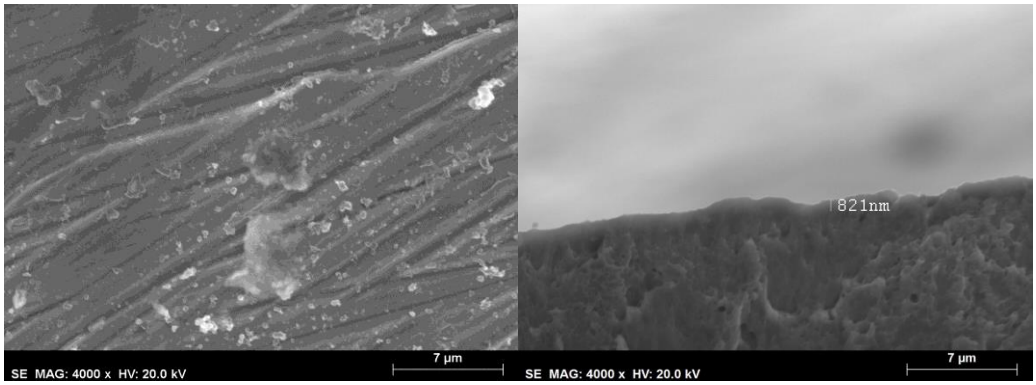

Figure 20 - SEM of the top (left) and cross-section (right) of the sample of reaction set 3 done using $2x10^{-1}$M of $K_2S_2O_8$.

By analysing the SEM images it is possible to observe that the concentration of $K_2S_2O_8$ has an effect on the thickness and the number and morphology of particles formed on top of the films.

The reactions done with $1x10^{-2}$M and $2x10^{-1}$M of $K_2S_2O_8$ yielded: high numbers of small particles; the roughest film surfaces; and the thickest films. Using $1x10^{-1}$M of $K_2S_2O_8$ yielded: big particles but in a smaller number which have PANI crystals inside an amorphous matrix; a smooth film surface; and an intermediate film thickness.

By comparing the morphology information with the measured specific capacitances we can understand that the film thickness has an important impact in the electrochemical specific capacitance of the electrodes. It is possible that the number of particles and roughness of the surface also have an impact in this characteristic. Namely, rougher surfaces and small particles in a high number increase the specific capacitance of the electrodes.

5.4. Reaction Set 4 – Aniline Concentration

In this reaction set the effect of aniline concentration was studied. As can be seen in the following table the highest deposited mass was obtained with $1x10^{-1}$M of aniline. This data also indicates that aniline concentrations above $1x10^{1}$M or under $1x10^{-4}$M are inadequate for PANI deposition by self-assembly on AISI304 stainless steel.

Table 16 - Mass of deposit self-assembled over the AISI304L stainless steel substrate per unit of sample area.

Set	Variable Tested	[Aniline] /M	Deposited Mass/Sample Area /g.cm^{-2}
4	Aniline Concentration	$1x10^{-3}$	Below detection limit
		$1x10^{-2}$	$2.27x10^{-6}$
		$1x10^{-1}$	$1.74x10^{-5}$
		1	$8.77x10^{-6}$
		$1x10^{1}$	Below detection limit

The composition of the coating formed on the surface of each sample was analyzed by Raman microscopy revealing very different spectra. The analysis of spectra from the samples made with any concentrations other than $1x10^{-2}$M, is difficult given the low peak intensity. This is probably due to the low deposited masses.

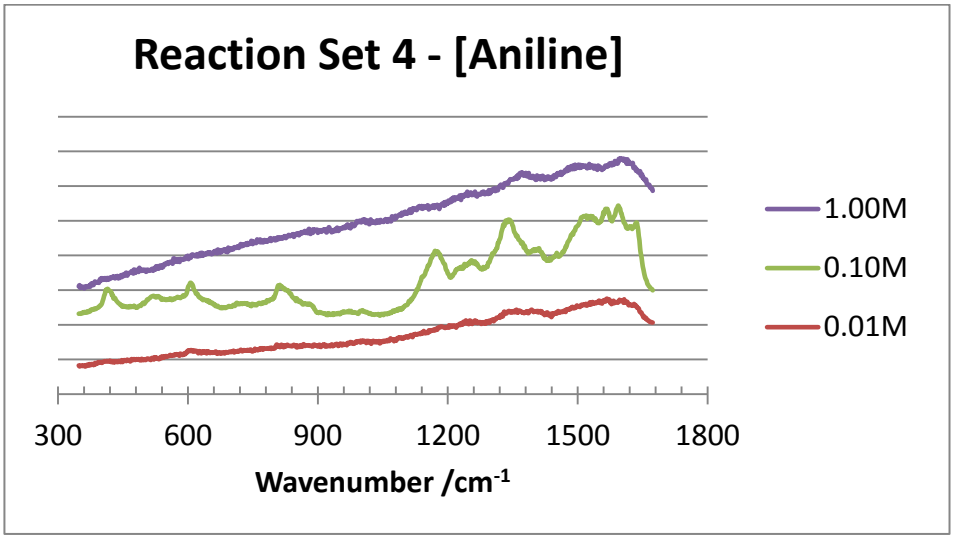

Figure 21 – Raman spectra of the surface of the AISI304L stainless steel samples exposed to the reactions of set 4.

The spectrum made with $1x10^{-1}$M of aniline has already been described above (reaction set 2, using $K_2S_2O_8$ as oxidizing species). Regarding the other samples we cannot draw any conclusions about their composition from their spectra.

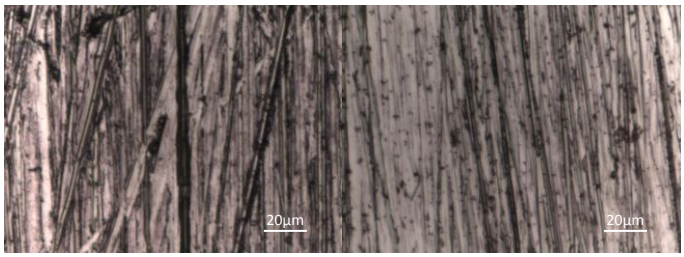

Figure 22 - Photos taken with the Raman microscope (50x magnification) of the surface of the samples from the reactions with $1x10^{-2}$M (left) and 1M of aniline.

From the photos taken of the surface of the samples it is possible to observe that all the reactions which yielded a measurable mass, had formed PANI polymer in the emeraldine base state (blue color). In the reactions done with $1x10^{-2}$M and 1M the emeraldine base is visible in the particle agglomerations at the surface and the coating formed inside the scratches of the surface.

Electrochemical charaterization of the samples was done, revealing the following electrochemical specific capacitances and potential ranges with capacitive behaviour.

Table 17 - Potential intervals and specific capacitances of the deposits formed on the surface of the AISI304L stainless steel samples exposed to the reactions of set 4.

[Aniline] /M	Film Thickness /nm	Potential Window /V	Specific Capacitance /$F.g^{-1}$
$1x10^{-2}$	471	-0.45 to 0.33	$7.41x10^{1}$
$1x10^{-1}$	238	-0.30 to 0.15	$1.94x10^{-3}$
1	143	-0.43 to 0.22	$1.63x10^{1}$

Thus, the aniline concentration which yields the best performing capacitor is $1x10^{-2}$M.

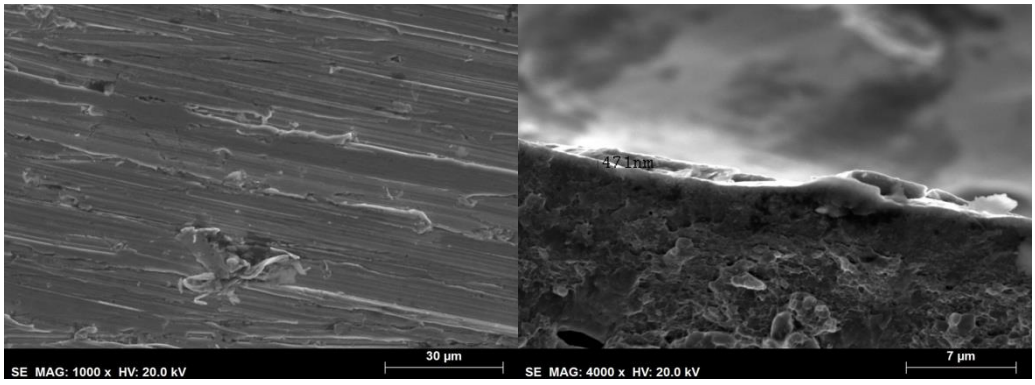

Figure 23 - SEM of the top (left) and cross-section (right) of the sample of reaction set 4 done using $1x10^{-2}$M of Aniline.

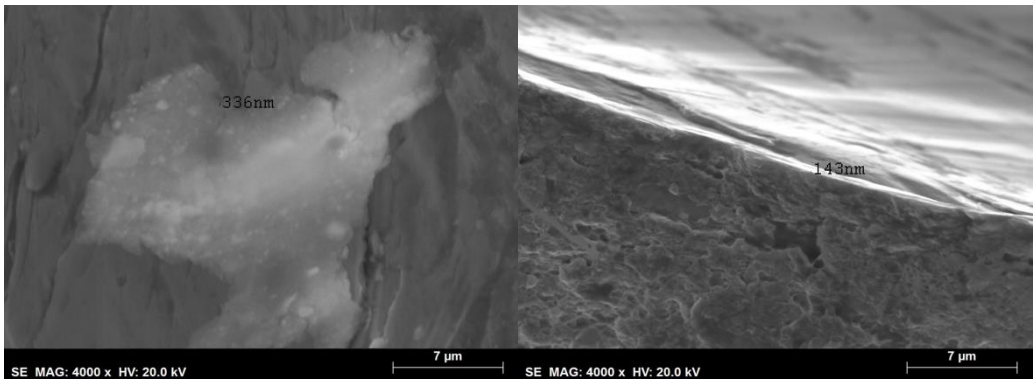

Figure 24 - SEM of the top (left) and cross-section (right) of the sample of reaction set 4 done using 1M of Aniline.

By analysing the SEM images it is possible to observe that the concentration of aniline has an important effect on the thickness and homogeneity of the coating and the total deposited mass.

The reaction done with $1x10^{-2}$M of aniline yields a small number of particles which are mainly concentrated around the surface defects of the substrate. The reaction carried out with 1M of aniline produces big PANI particles composed of small crystals surrounded by amourphous regions. Both reactions done with $1x10^{-2}$M and 1M of aniline produce films with 471nm and 143nm of thickness, respectively.

By comparing the morphology information with the measured specific capacitances we can understand that despite the thickest and most homogeneous film being that done using $1x10^{-1}$M of aniline it is the one which present the smallest specific capacitance. This could be due to the bigger exposed steel surface which contributed to the capacitive behaviour and/or the surface area of the particles on the surface.

5.5. Reaction Set 5 – Phosphoric Acid Concentration

In this reaction set, the effect of phosphoric acid concentration was studied. As can be seen in the following table the highest deposited mass was obtained with $5x10^{-2}$M of H_3PO_4.

Table 18 - Mass of deposit self-assembled over the AISI304L stainless steel substrate per unit of sample area.

Set	Variable Tested	$[H_3PO_4]$ /M	Deposited Mass/Sample Area ($g.cm^{-2}$)
5	H_3PO_4 Concentration	$5x10^{-4}$	$1.27x10^{-5}$
		$5x10^{-3}$	$8.50x10^{-6}$
		$5x10^{-2}$	$1.74x10^{-5}$
		$5x10^{-1}$	$7.67x10^{-6}$
		5	$1.25x10^{-6}$

The composition of the coating formed on the surface of each sample was analyzed by Raman microscopy revealing very similar spectra. The main differences are in the relative intensity and in slight wavelength shifts of some peaks.

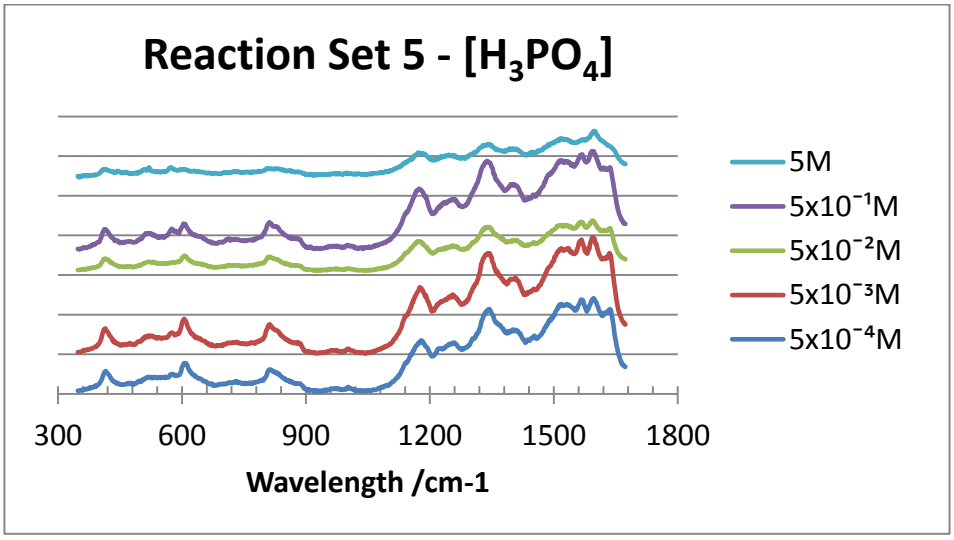

Figure 25 - Raman spectra of the surface of the AISI304L stainless steel samples exposed to the reactions of set 5.

In all these Raman spectra it is possible to observe peaks which indicate the formation of aniline oligomers and/or polymer. Namely at 412cm^{-1} for 5x10^{-1}M, at 414cm^{-1} for 5x10^{-3}M and 5x10^{-2}M and 416cm^{-1} for 5x10^{-4}M and 5M, which correspond to the phenazine's C-H and/or C-N-C out-of-plane wag and torsion. Other related peaks are visible at 1338cm^{-1} for 5x10^{-4}M and 1340cm^{-1} for the other concentrations, for the C~N^{+} stretch on phenazine or safranine-like segments; and at 1618cm^{-1} for 5M, 1621cm^{-1} for 5x10^{-4}M, 5x10^{-3}M and 5x10^{-1}M, and 1623cm^{-1} for 5x10^{-2}M for the C~C wag of the benzenoid ring.

The Raman spectra also confirm the presence of sulfate ions by their visible peaks at 605cm^{-1} for 5x10^{-4}M, 5x10^{-3}M and 5M, 607cm^{-1} for 5x10^{-2}M and 603cm^{-1} for 5x10^{-1}M of phosphoric acid. All spectra show peaks of the phosphate P-O stretch vibrations in the 900-1000cm^{-1} region.

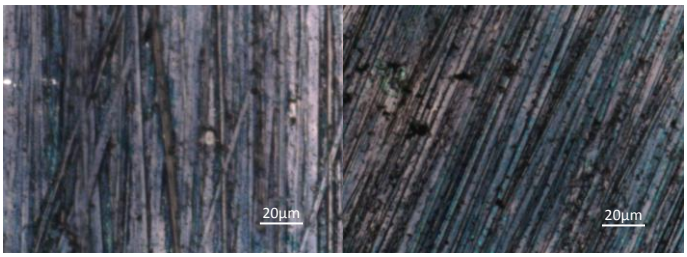

Figure 26 - Photos taken with the Raman microscope (50x magnification) of the surface of the samples from the reactions with 5x10^{-4}M (left) and 5x10^{-3}M (right) of H_3PO_4.

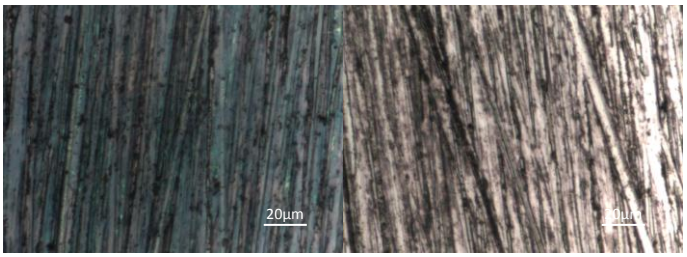

Figure 27 - Photos taken with the Raman microscope (50x magnification) of the surface of the samples from the reactions with $5x10^{-1}$M (left) and 5M (right) of H_3PO_4.

From the photos of the surface of the samples, together with the Raman data, it is possible to assume that the reactions made with $5x10^{-4}$M and $5x10^{-3}$M of H_3PO_4, both formed a film of PANI polymer in the emeraldine base state (blue color), and with $5x10^{-1}$M and 5M emeraldine (green color) state. In the last sample the film is visible macroscopically and microscopically within the scratches on the surface.

Electrochemical characterization of the samples was done, revealing the following electrochemical specific capacitances and potential ranges with capacitive behaviour.

Table 19 - Potential intervals and specific capacitances of the deposits formed on the surface of the AISI304L stainless steel samples exposed to the reactions of set 5.

$[H_3PO_4]$ /M	Film Thickness /nm	Potential Range /V	Specific Capacitance /$F.g^{-1}$
$5x10^{-4}$	228	-0.45 to 0.25	$1.14x10^{1}$
$5x10^{-3}$	178	-0.40 to 0.10	$1.80x10^{1}$
$5x10^{-2}$	238	-0.30 to 0.15	$1.94x10^{-3}$
$5x10^{-1}$	1130	-0.40 to 0.20	$1.83x10^{-1}$
5	135	-0.40 to 0.20	$3.41x10^{2}$

Thus, the phosphoric acid concentration which yields the best performing capacitor is 5M.

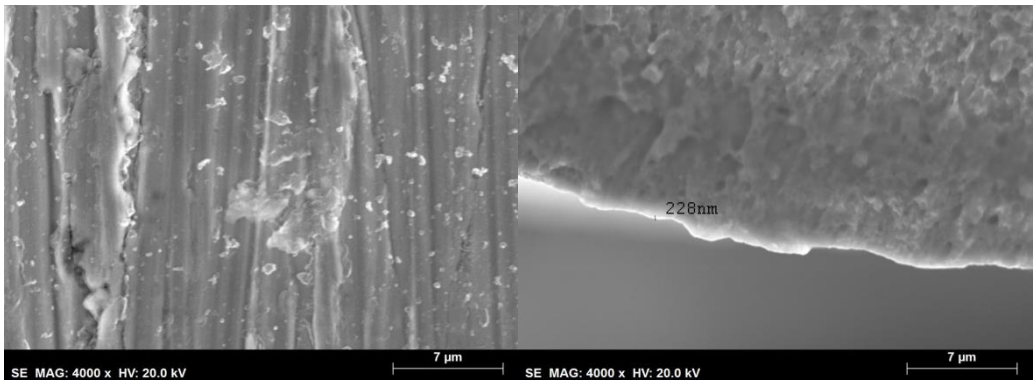

Figure 28 - SEM of the top (left) and cross-section (right) of the sample of reaction set 5 done using $5x10^{-4}$M of H_3PO_4.

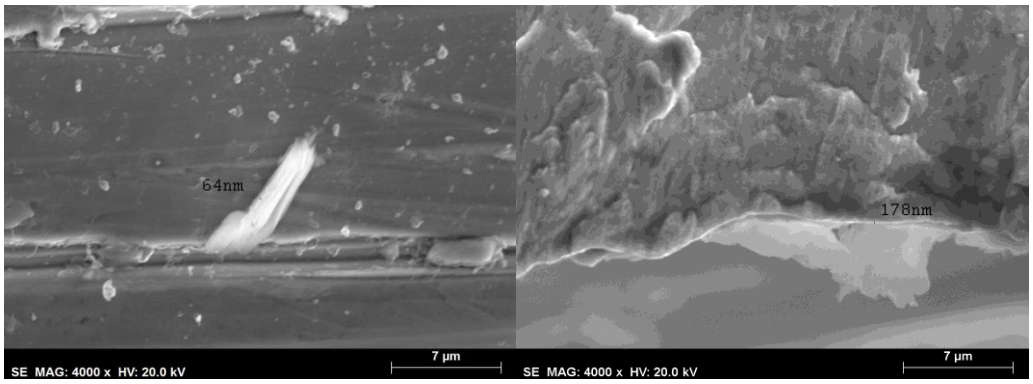

Figure 29 - SEM of the top (left) and cross-section (right) of the sample of reaction set 5 done using $5x10^{-3}$M of H_3PO_4.

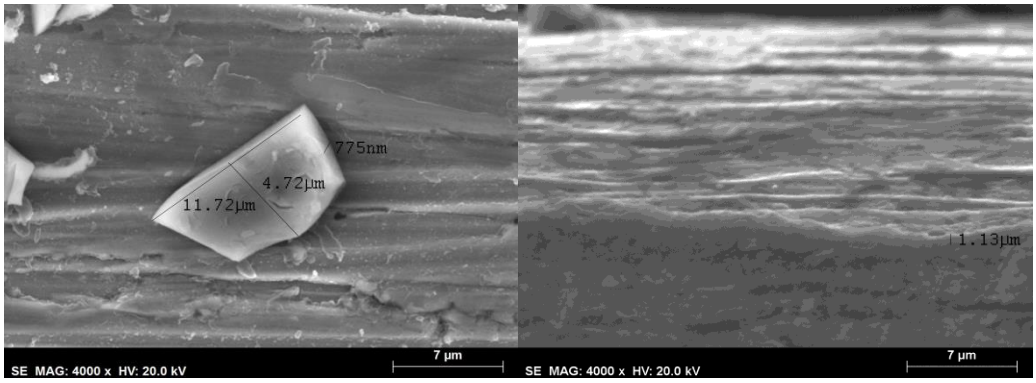

Figure 30 - SEM of the top (left) and cross-section (right) of the sample of reaction set 5 done using $5x10^{-1}$M of H_3PO_4.

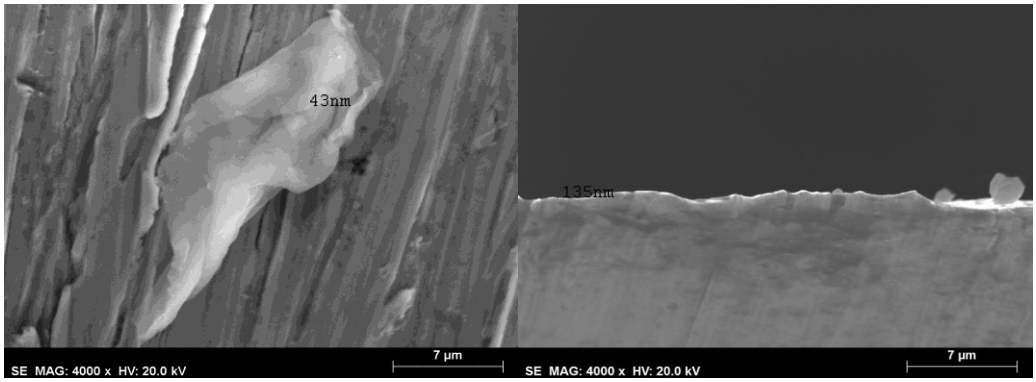

Figure 31 - SEM of the top (left) and cross-section (right) of the sample of reaction set 5 done using 5M of H_3PO_4.

By analysing the SEM images it is possible to observe that the concentration of H_3PO_4 has an important effect on the film thickness and the number and morphology of the particles at its surface.

With $5x10^{-4}$M of H_3PO_4 we get a high number of small sized particles on top of a film with 228nm of thickness. By increasing ten times the concentration to $5x10^{-3}$M we get a lower number of particles, with a bigger dimension and a stacked nanosheet morphology. The film thickness is of 178nm and of the nanosheets 64nm. In the reference reaction conditions we get

the previously mentioned 238nm thick film, and more particles of smaller and similar sizes and thickness, but with a folded nanosheet morphology. The reaction done using $5x10^{-1}$M of H_3PO_4 originates small numbers of rectangular particles, similar to those obtained in reaction set 3 using $1x10^{-1}$M of aniline. The film from this reaction is also the thickest, with 1.13µm. The reaction with the highest phosphoric acid concentration gave both the thinnest film, with 135nm and a small number of big particles with nanosheet morphology and 43nm of thickness. In these nanosheets there are no clearly defined amorphous and crystalline regions.

By comparing the morphology information with the measured electrochemical specific capacitances we can understand that the coating thickness by itself is not the determining element in the value of the electrochemical specific capacitance of the electrode. Other important elements are the particle number, morphology (higher capacitances if nanosheet), texture homogeneity (no clear distinction between amorphous and crystalline phases) and size (higher values if bigger sizes of the nanosheets).

5.6. Reaction Set 6 – Sulfuric Acid Concentration

In this reaction set, the effect of sulfuric acid concentration was studied. As can be observed in the following table, the highest deposited mass was obtained with $5x10^{-3}$M of H_2SO_4.

Table 20 - Mass of deposit self-assembled over the AISI304L stainless steel substrate per unit of sample area.

Set	Variable Tested	$[H_2SO_4]$ /M	Deposited Mass/Sample Area /g.cm^{-2}
6	H_2SO_4 Concentration	$5x10^{-4}$	$3.67x10^{-5}$
		$5x10^{-3}$	$3.82x10^{-5}$
		$5x10^{-2}$	$1.74x10^{-5}$
		$5x10^{-1}$	$1.22x10^{-6}$
		5	$1.00x10^{-6}$

The composition of the coating formed on the surface of each sample was analyzed by Raman microscopy revealing very similar spectra. The main differences are in the relative intensity and slight shifts in the wavelength of some peaks.

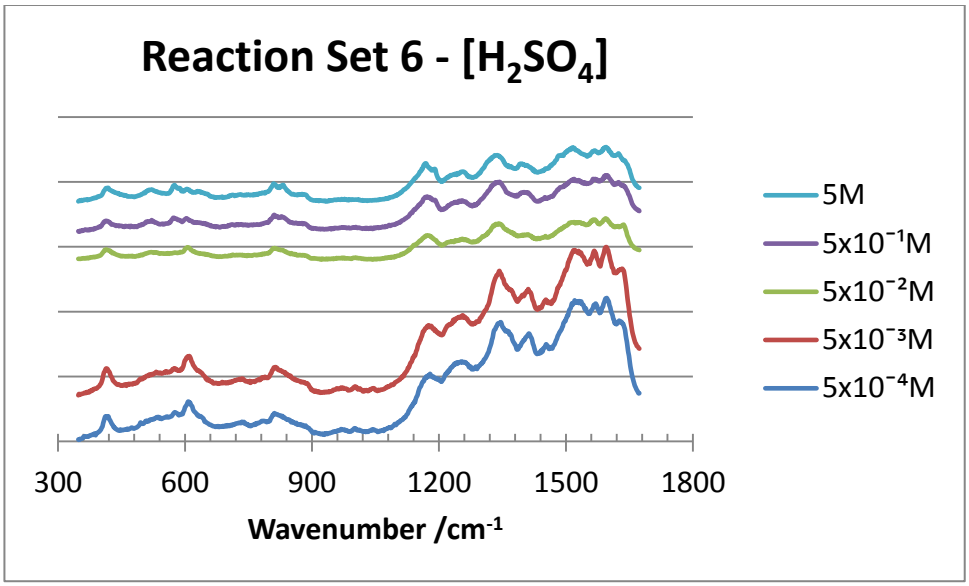

Figure 32 - Raman spectra of the surface of the AISI304L stainless steel samples exposed to the reactions of set 6.

In all these Raman spectra it is possible to observe peaks which indicate the formation of aniline oligomers and/or polymers. Namely at 412cm^{-1} for 5x10^{-4}M and at 414cm^{-1} for the other H_2SO_4 concentrations which correspond to the phenazine's C-H and/or C-N-C out-of-plane wag and torsion. Other related peaks are visible at 1338cm^{-1} for 5M, 1340cm^{-1} for 5x10^{-4}M, 5x10^{-2}M , 5x10^{-1}M and 1343cm-1 for 5x10^{-3}M. These are related with the C~N^{+} stretch on phenazine or safranine-like segments. At 1617cm^{-1} for 5x10^{-4}M, 1620cm^{-1} for 5x10^{-3}M, 1623cm^{-1} for 5x10^{-2}M and 1624cm^{-1} for 5x10^{-1}M and 5M, we have the peaks from the C~C wag of the benzenoid ring.

The Raman spectra also confirm the presence of sulfate ions by their visible peaks at 603cm^{-1} for 5x10^{-1}M, 605cm^{-1} for 5M, 607cm^{-1} for 5x10^{-2}M and 5x10^{-3}M, and 608cm-1 for 5x10^{-4}M of sulphuric acid. All spectra show the peaks of the phosphate P-O stretch vibrations in the 900-1000cm^{-1} region.

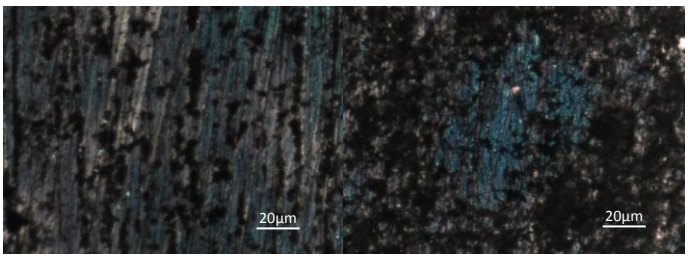

Figure 33 - Photos taken with the Raman microscope (50x magnification) of the surface of the samples from the reactions with 5x10^{-4}M (left) and 5x10^{-3}M (right) of H_2SO_4.

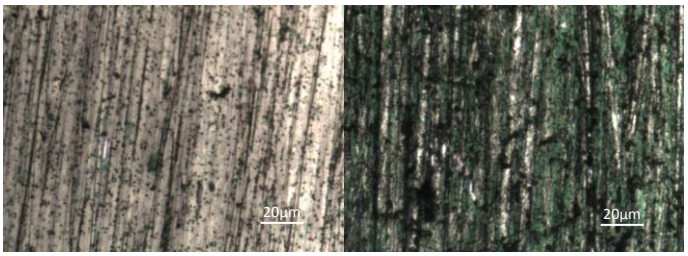

Figure 34 - Photos taken with the Raman microscope (50x magnification) of the surface of the samples from the reactions with $5x10^{-1}$M (left) and 5M (right) of H_2SO_4.

From the photos of the surface of the samples, together with the Raman data, it is possible to assume that the reactions made with $5x10^{-4}$M and $5x10^{-3}$M of H_2SO_4, both formed a film of aniline polymer in the emeraldine base state (blue color), and with $5x10^{-1}$M and 5M emeraldine (green color) state.

Electrochemical characterization of the samples was done, revealing the following electrochemical specific capacitances and potential ranges with capacitive behaviour.

Table 21 - Potential intervals and specific capacitances of the deposits formed on the surface of the AISI304L stainless steel samples exposed to the reactions of set 6.

$[H_2SO_4]$ /M	Film Thickness /nm	Potential Range /V	Specific Capacitance /F.g^{-1}
$5x10^{-4}$	1880	-0.35 to 0.45	$3.88x10^{1}$
$5x10^{-3}$	2020	0.28 to 0.55	$1.82x10^{1}$
$5x10^{-2}$	238	-0.30 to 0.15	$1.94x10^{-3}$
$5x10^{-1}$	1660	0.00 to 0.45	$4.44x10^{2}$
5	6550	-0.40 to 0.20	$2.24x10^{3}$

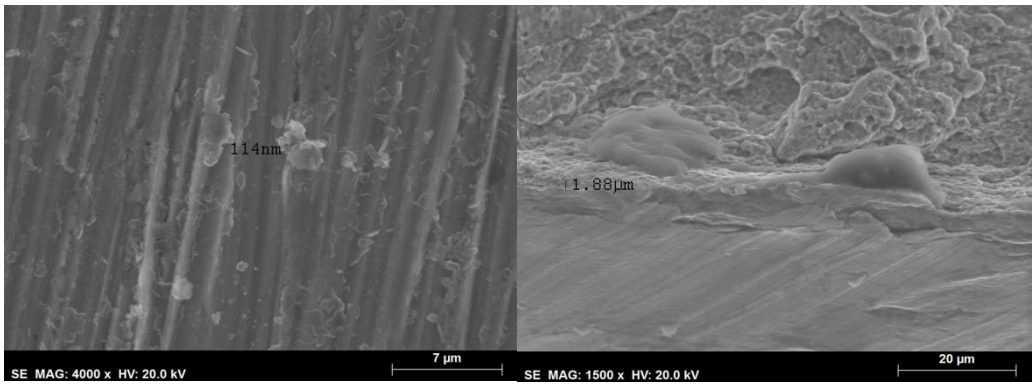

Figure 35 - SEM of the top (left) and cross-section (right) of the sample of reaction set 6 done using $5x10^{-4}$M of H_2SO_4.

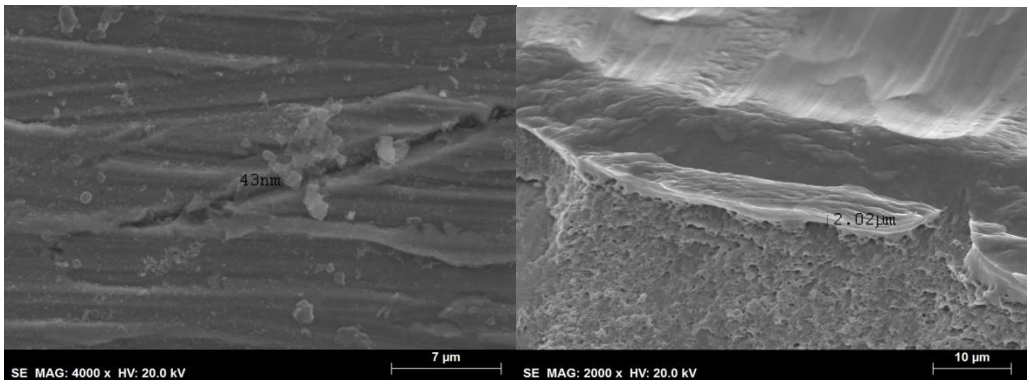

Figure 36 - SEM of the top (left) and cross-section (right) of the sample of reaction set 6 done using $5x10^{-3}$M of H_2SO_4.

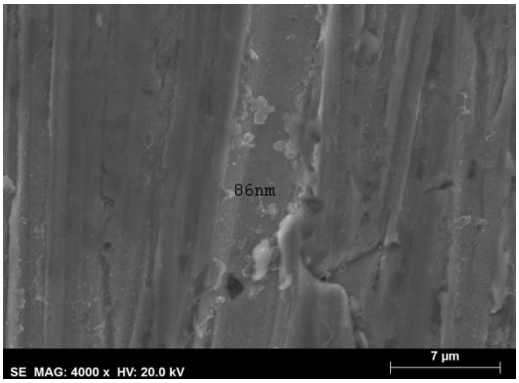

Figure 37 - SEM of the top (left) of the sample of reaction set 6 done using $5x10^{-1}$M of H_2SO_4.

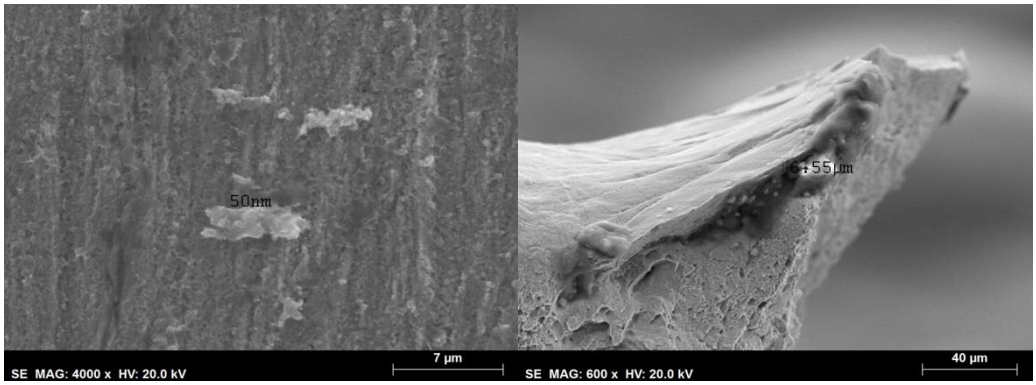

Figure 38 - SEM of the top (left) and cross-section (right) of the sample of reaction set 6 done using 5M of H_2SO_4.

By analysing the SEM images it is possible to observe that the concentration of H_2SO_4 has an important effect on the morphology of the films.

With the lowest tested sulphuric acid concentration the film deposited is 1.88µm thick and has a rough surface with many small sized particles having a nanosheet morphology (with 114nm of thickness). By increasing the concentration of H_2SO_4 by ten times, the film thickness increased to 2.02µm. Moreover, the number of particles on its surface decreases as well as size and thickness (43nm). These particles have a nanosheet morphology. The reference sample has

a much thinner (238nm) film with nanosheet particles in higher numbers and bigger sizes. The electrode prepared using $1x10^{-1}$M of H_2SO_4 has a smaller number of nanoparticles with a nanosheet morphology of 86nm of thickness. Unfortunately to ascertain the thickness of the coating itself new SEM images must be taken of the cross-section. However by analysing the Raman microscopy image we can assume that this will be thin and heterogeneous in distribution. The reaction done using 5M H_2SO_4 yielded the thickest coating of this study with 6.55µm with a very rough surface, and porous structure and particles.

By comparing the morphology information with the measured specific capacitances we can understand that overall, the thicker the coating, the higher the electrochemical specific capacitance of the electrode. The same correlation is observed concerning the porosity of the coating. However these morphological characteristics alone do not justify the measured capacitances of the electrodes. If we relate the SEM data with the Raman microscopy photos we notice that the electrodes with the highest specific capacitances are those with the aniline polymer in the green emeraldine oxidation state, which is the conductive form of PANI. Thus we can assume that both the morphological and chemical oxidation state of the PANI deposited on the stainless steel surface are responsible for these high specific capacitance values.

The electrochemical specific capacitance of the sample done using 5M of sulfuric acid, is higher than the theoretical value of $2x10^{3}F.g^{-1}$ for PANI alone. Despite the electrode made being a composite of PANI and stainless steel, this is a very high value. Thus it is possible that there is an error in the mass of PANI measured, which would be responsible for this high value.

5.7. Reaction Set 7 – Reaction Time

In this reaction set, the effect of reaction time was studied. As can be seen in the following table, the highest deposited mass was obtained with 24 hours of reaction.

Table 22 - Mass of deposit self-assembled over the AISI304L stainless steel substrate per unit of sample area.

Set	Variable Tested	Time /h	Deposited Mass/Sample Area /g.cm^{-2}
7	Reaction time	2	$5.03x10^{-6}$
		4	$1.09x10^{-6}$
		16	$6.13x10^{-6}$
		24	$1.74x10^{-5}$
		38	$1.36x10^{-6}$
		48	$9.97x10^{-6}$

The composition of the deposit formed on the surface of each sample was analyzed by Raman microscopy revealing very similar spectra. The main differences are in the peak intensity and slight shifts in the wavelength of some peaks.

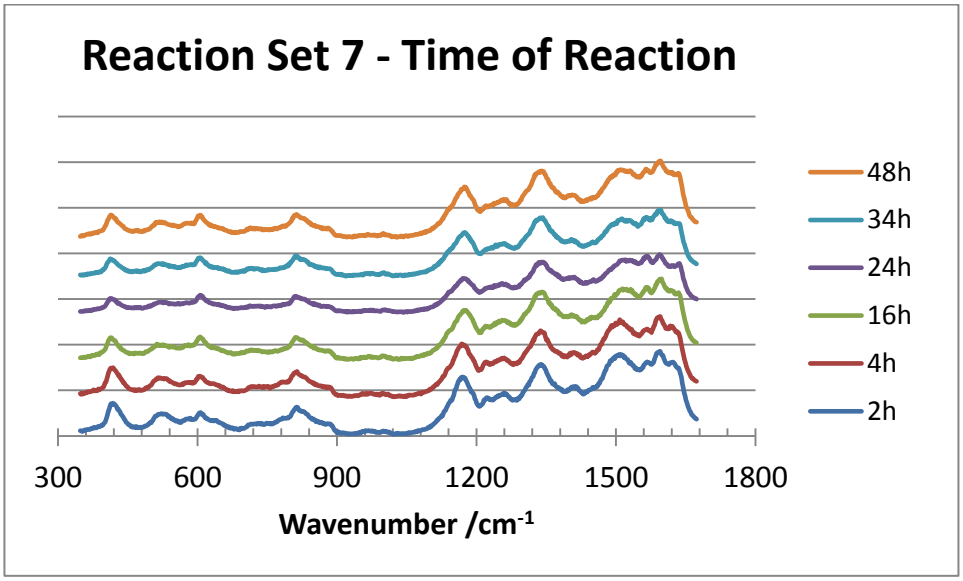

Figure 39 - Raman spectra of the surface of the AISI304L stainless steel samples exposed to the reactions of set 7.

In all these Raman spectra we can see peaks which indicate the formation of aniline oligomers and/or polymer. Namely at 412cm^{-1} for 16h and 34h, at 414cm^{-1} for 4h, 24h and 48h, and at 416cm^{-1} for 2 hour-long reactions related with the phenazine's C-H and/or C-N-C out-of-plane wag and torsion. Other related peaks are visible at 1338cm^{-1} for 4h, 1340cm^{-1} for 2h and 24h, 1341cm^{-1} for 16h and 48h, and 1343 cm^{-1} for 34h. These are related with the C~N^{+} stretch on phenazine or safranine-like segments. At 1621cm^{-1} for 4h and 1623cm^{-1} for the other reaction times we have the peaks from the C~C wag of the benzenoid ring.

The Raman spectra also confirm the presence of sulfate ions by their visible peaks at 605cm^{-1} for 4h, 16h and 34h, and 607cm-1 for 2h, 24h and 48h reactions. All spectra show peaks of the phosphate P-O stretch vibrations in the 900-1000cm^{-1} region.

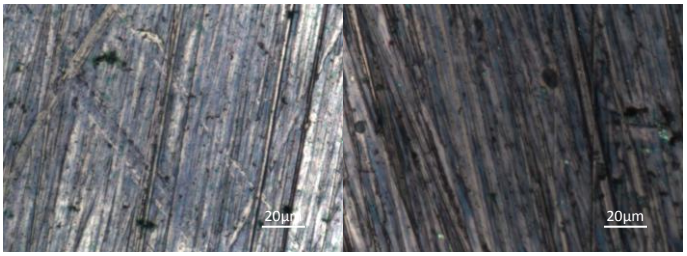

Figure 40 - Photos taken with the Raman microscope (50x magnification) of the surface of the samples from the reactions done during 2 hours (left) and 4 hours (right).

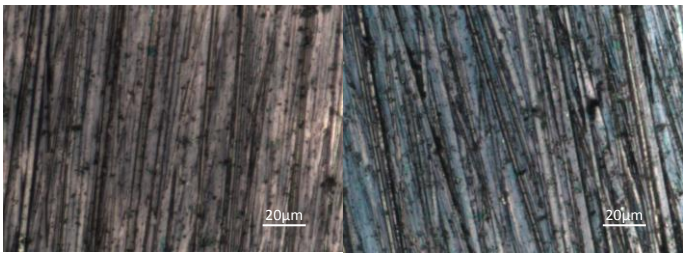

Figure 41 - Photos taken with the Raman microscope (50x magnification) of the surface of the samples from the reactions done during 16 hours (left) and 34 hours (right).

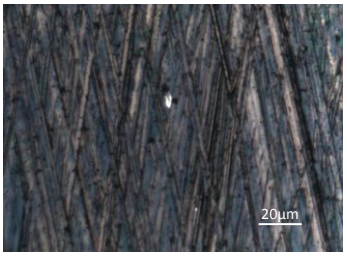

Figure 42 - Photos taken with the Raman microscope (50x magnification) of the surface of the samples from the reactions done during 48 hours.

From the photos of the surface of the samples, together with the Raman data, it is possible to assume that in all the reactions a film of PANI in the emeraldine base state (blue color) was formed.

Electrochemical characterization of the samples was done, revealing the following electrochemical specific capacitances and potential ranges with capacitive behaviour.

Table 23 - Potential intervals and specific capacitances of the deposits formed on the surface of the AISI304L stainless steel samples exposed to the reactions of set 7.

Reaction Time /h	Film Thickness /nm	Potential Range /V	Specific Capacitance /F.g^{-1}
2	114	0.15 to 0.55	$1.23x10^{1}$
4	879	0.15 to 0.55	$1.63x10^{3}$
16	543	-0.25 to 0.40	$3.69x10^{1}$
24	238	-0.30 to 0.15	$1.94x10^{-3}$
34	721	-0.45 to 0.35	$2.10x10^{2}$
48	1170	-0.40 to 0.25	$2.82x10^{1}$

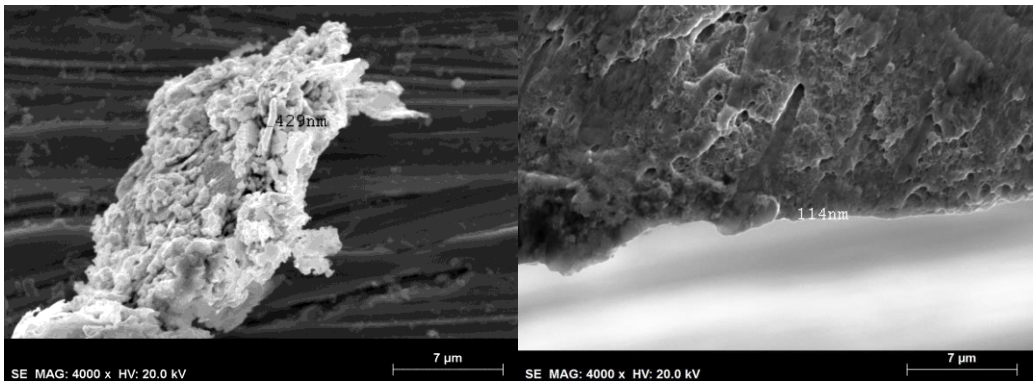

Figure 43 - SEM of the top (left) and cross-section (right) of the sample of reaction set 7 done in 2 hours.

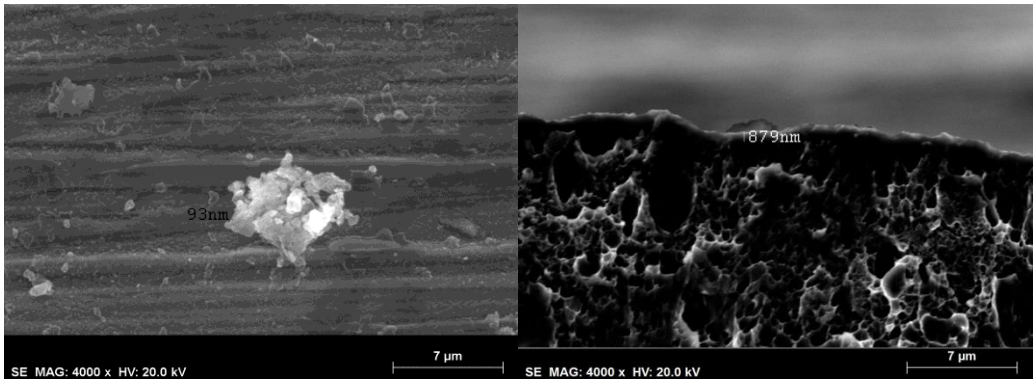

Figure 44 - SEM of the top (left) and cross-section (right) of the sample of reaction set 7 done in 4 hours.

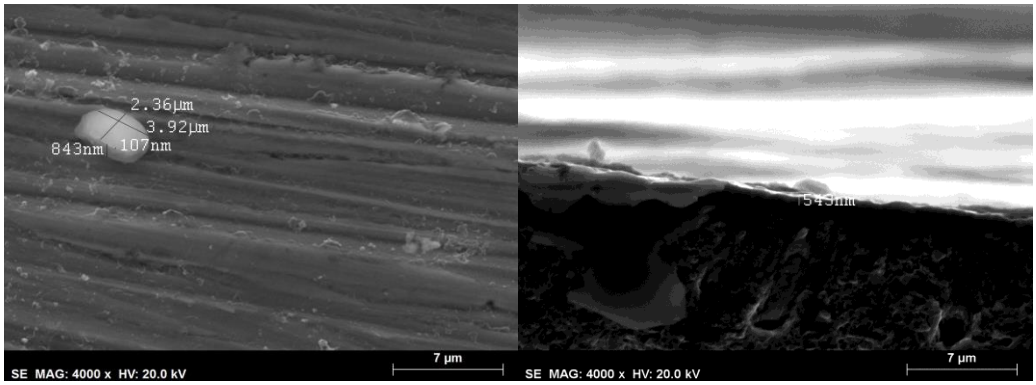

Figure 45 - SEM of the top (left) and cross-section (right) of the sample of reaction set 7 done in 16 hours.

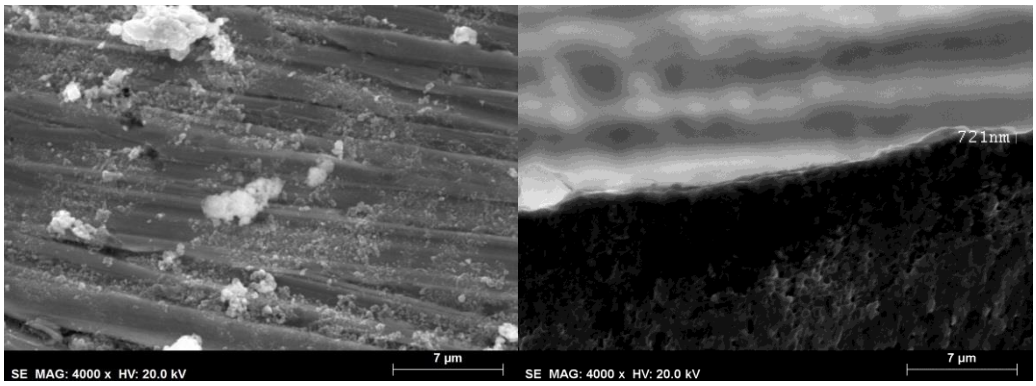

Figure 46 - SEM of the top (left) and cross-section (right) of the sample of reaction set 7 done in 34 hours.

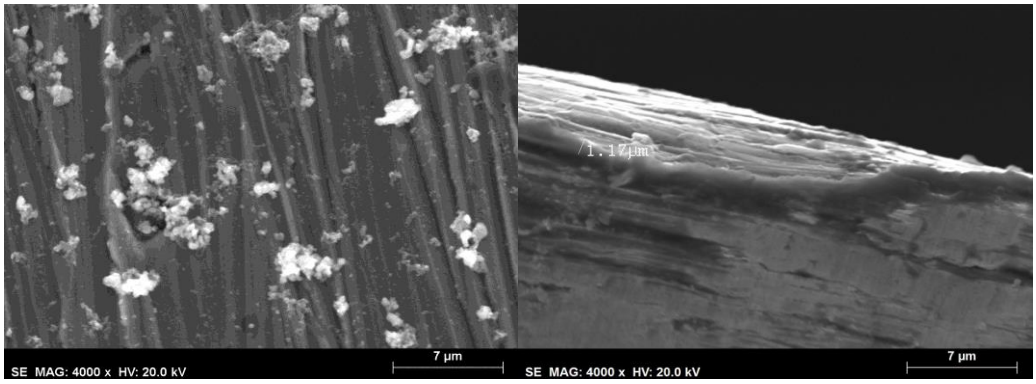

Figure 47 - SEM of the top (left) and cross-section (right) of the sample of reaction set 7 done in 48 hours.

By analysing the SEM images we can understand that the reaction time has an important effect on the thickness and morphology of the films and particles.

After 2 hours of reaction we get a 114nm thick film showing big agglomerates of particles. The surface of the film is also filled with other small nanosheet-like particles. The electrode done with 4 hours of reaction has a thicker 879nm film with a rough surface and nanosheet particles on top. At this reaction time there are still some particle agglomerates, but with much smaller sizes. A 16 hour-long reaction yields a thinner 549nm film with a smoother surface. There are also less small nanosheet particles on the surface and some are bigger nanosheet stacks. These nanosheets are 107nm thick. The reference reaction is 24 hour-long and has been described previously as yielding a thinner 238nm smoother film and almost no particles on the surface. After 36 hours of reaction the film formed increases its thickness to 721nm and surface roughness with many particle agglomerations of various sizes. The longest reaction time tested yielded a thicker 1.17µm and smoother film smoother surface with a globular particles agglomerations with a more homogeneous size distribution.

By comparing the morphology information with the measured specific capacitances we can understand that the most important variables are the thickness of the films, roughness of the surface, and the number and nanosheet morphology of the particles.

5.8. Reaction Set 8 – Metallic Oxides Addition

In this reaction set, the effect of the addition of metallic oxide particles was studied. As can be seen in the following table, the highest deposited mass was obtained with ZnO.

In this reaction set the metallic oxide particles were added and stirred during the same reaction time. The goal was to coat these with PANI and acertain if the core-shell particles created would deposit over or under the surface film. The metallic oxides chosen were ZnO and MnO_2 since the first is known to be an n-type semiconductor[51] and the later a good electric conductor[52].

Table 24 - Mass of deposit self-assembled over the AISI304L stainless steel substrate per unit of sample area.

Set	Variable Tested	Species	Deposited Mass/Sample Area /g.cm^{-2}
	Metallic Oxide Particle Addition	-	$1.74x10^{-5}$
		ZnO	$3.92x10^{-5}$
		MnO_2	$3.50x10^{-7}$

Raman microscopy was used to analyse the composition of the coating formed on the surface of each sample. To try and determine if the metallic oxides used during the synthesis were part of this deposit, Raman spectra of these were taken and compared.

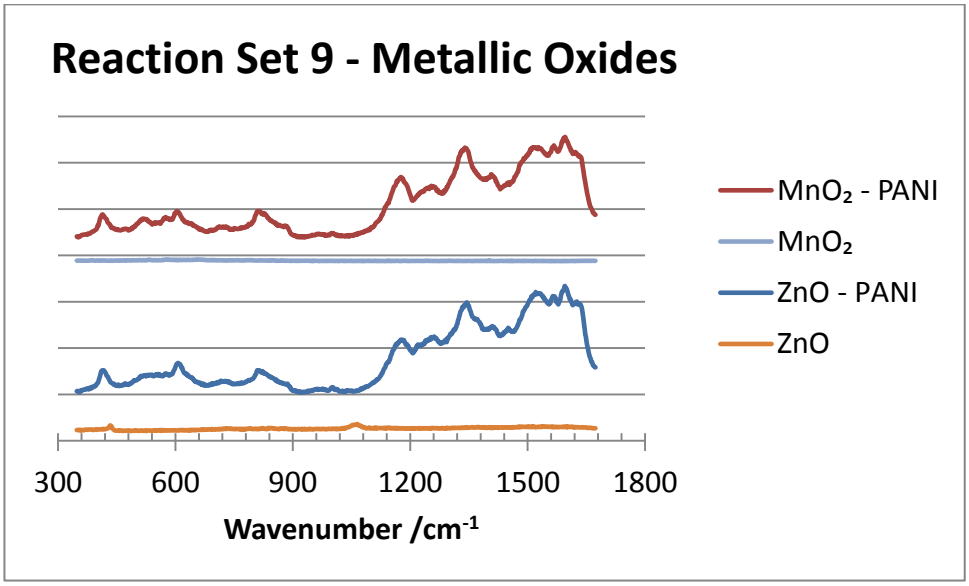

Figure 48 - Raman spectra of the surface of the AISI304L stainless steel samples exposed to the reactions of set 8 and of the metallic oxides used.

The Raman spectra of the reactions done with either of the metallic oxides does not allow to make any assumptions regarding the inclusion of these in the electrodes. The spectra were taken in a larger frequency range than the one displayed, however no further information

can be inferred from it. The deposits from these reactions do not include the added metallic oxides since their cyclic voltammograms did not have their characteristic oxidation and reduction peaks.

The Raman spectra of all the reaction sample surfaces have peaks which indicate the formation of aniline oligomers and/or polymer. Namely at 414cm^{-1} with ZnO and MnO_2 for the peak related with the phenazine's C-H and/or C-N-C out-of-plane wag and torsion. Other related peaks are visible at 1338cm^{-1} for ZnO and 1340cm^{-1} for MnO_2, related with the C~N^{+} stretch on phenazine or safranine-like segments. At 1621cm^{-1} for MnO_2 and 1626cm^{-1} for ZnO we have the peaks from the C~C wag of the benzenoid ring.

The Raman spectra also confirm the presence of sulfate ions by their visible peaks at 603cm^{-1} with MnO_2 and 607cm^{-1} with ZnO. All spectra show peaks of the phosphate P-O stretch vibration in the 900-1000cm^{-1} region.

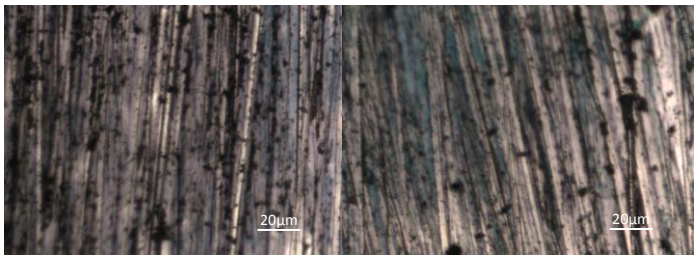

Figure 49 - Photos taken with the Raman microscope (50x magnification) of the surface of the samples from the reactions done using ZnO (left) and MnO_2 (right).

From the photos of the surface of the samples, together with the Raman data, we are able to say that in all the reactions a film of PANI polymer in the emeraldine base state (blue color) was formed.

Electrochemical characterization of the samples was done, revealing the following electrochemical specific capacitances and potential ranges with capacitive behaviour. The highest capacitance was observed with MnO_2 which is an oxide commonly used in redox supercapacitors.

Table 25 - Potential intervals and specific capacitances of the deposits formed on the surface of the AISI304L stainless steel samples exposed to the reactions of set 8.

Metallic Oxide	Film Thickness /nm	Potential Range /V	Specific Capacitance /F.g^{-1}
-	238	-0.30 to 0.15	1.94x10^{-3}
ZnO	721	-0.43 – 0.33	4
MnO_2	821	0.25 – 0.75	1.60x10^{2}

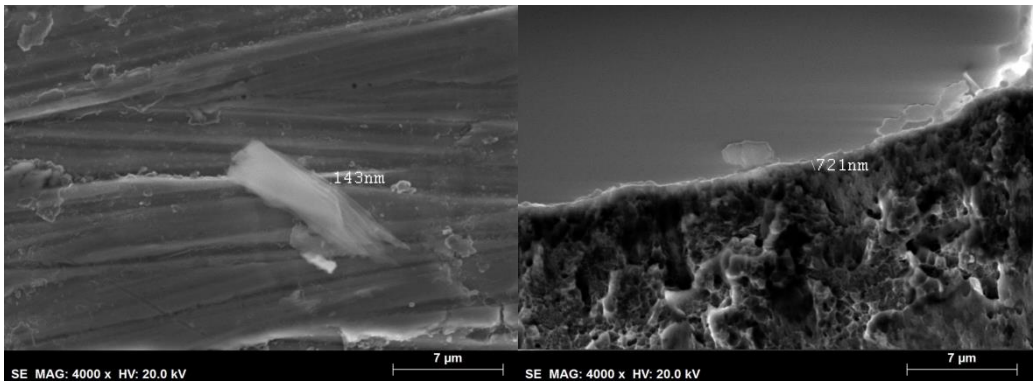

Figure 50 - SEM of the top (left) and cross-section (right) of the sample of reaction set 8 done with ZnO.

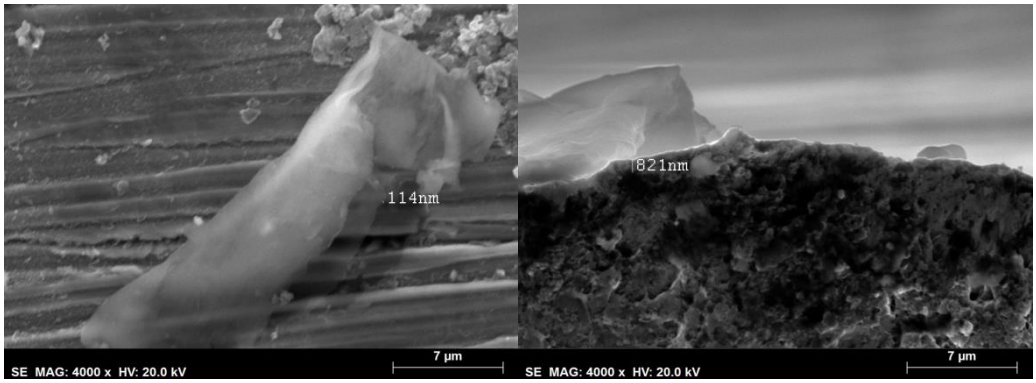

Figure 51 - SEM of the top (left) and cross-section (right) of the sample of reaction set 8 done with MnO_2.

By analysing the SEM images we can see that the addition of metallic oxides in the reaction medium has an effect on the thickness and morphology of the surface and particles.

The reaction done with ZnO yielded nanosheet-like stacked particles with 143nm thickness on the surface of a smooth 721nm thick film . Using MnO_2 in the reaction medium also yielded more particles, with a sheet morphology, but not stacked and with a bigger dimension. The thickness of the film, with a rougher surface, was of 821nm.

By comparing the morphology information with the measured electrochemical specific capacitances we can understand that the most important variables for the different performances are the roughness of the film surface and the number, size and sheet morphology of the particles.

6. Conclusions

After the completion of this systematic study we understand the different impact different variables have on the electrochemical specific capacitance of electrodes of PANI on AISI304L stainless steel.

In the first reaction set we find that the lowest surface resistivities are obtained on the AISI304L stainless steel substrates. Between the different surface roughening procedures done to increase the surface area, the one which gave the lowest surface resistivity had been grinded with the coarsest 500 grit SiC paper.

In the second reaction set we found that the oxidant species had a crucial effect on the deposition on the surface of the stainless steel. From those tested, the only ones which yielded a measurable mass were NaClO and $K_2S_2O_8$. This gave the highest deposited mass and for that reason it was chosen as the oxidant for the following studies.

The third reaction set revealed that concentrations below $1x10^{-3}$M or above 1M of potassium persulfate yielded deposited masses too small to be measured. From the other concentrations the best electrochemical specific capacitances were obtained with $1x10^{-2}$M ($4.15x10^{1}F.g^{-1}$) and $2x10^{-1}$M ($1.59x10^{1}F.g^{-1}$) of $K_2S_2O_8$. These best performing electrodes were those with the thickest film, highest number of particles on the surface and roughest surface.

With the fourth reaction set, it was clear that the best aniline concentration to use was of $1x10^{-1}$M, given that any of the other concentrations either gave small deposited masses. Some of these were even too small to be measured.

In the fifth reaction set we found that despite the fact that the phosphoric acid concentration has an important effect on the on the number and morphology of the particles on the surface of the film. It is possible that the phosphoric acid promotes the nanosheet morphology, organization and number. As the H_3PO_4 concentration increases the average size of the particles does the same, their morphology starts to approach that of nanosheets and their numbers decrease. There is a critical concentration in which the particles and film synthesized are thick, which could be due to the stacking of the nanosheets. This would be promoted by π-π stacking. The highest specific capacitance of the electrode prepared using a 5M concentration could be partially due to the emeraldine oxidation state of PANI.

The higher specific capacitances from the films of PANI in the emeraldine oxidation state are also observed in the sixth reaction set where the effect of the sulfuric acid concentration was tested.This variable has a significant influence in the roughness of the surface of the coating. As the concentration increases, the surface roughness decreases, reaching the

smoothest at $5x10^{-2}$M of H_2SO_4. Above this concentration value the surface roughness increases again. At 5M of sulfuric acid, the specific capacitance obtained was of $2.24x10^{3}F.g^{-1}$. This value is higher than the theoretical value for PANI alone, $2x10^{3}F.g^{-1}$ and can have been obtained by mass loss during the assembly of the electrochemical cell.

Reaction set seven assessed the impact of reaction time. From the deposited masses we cannot ascertain if the observed differences come from chain length differences. As the reaction time increases the thickness and roughness of the film increases up to 4 hours of reaction. After longer periods these decrease until 24 hours of reaction, after which they increase once more. At 4 hours of reaction the electrochemical specific capacitance was the highest measured, $1.63x10^{3}F.g^{-1}$. This value is close to the highest available in the literature for PANI on AISI304L stainless steel, $1300F.g^{-1}$.[23]

The addition of metallic oxides on the reaction medium does not imply their inclusion in the formed coating. In fact no evidence was found of their inclusion on the electrodes done in reaction set eight. The effect of the addition of the tested metallic oxides (ZnO and MnO_2) is mainly on the roughness of the surface of the coating and on the size and number of the particles. These had a nanosheet morphology on both samples.

7. Future Work

After this work, a deeper understanding of the phenomena behind the high electrochemical specific capacitances obtained in some samples is necessary[53]. To achieve this electrochemical impedance spectroscopy (EIS) of these samples should be made. This technique will allow us to understand if the high capacitances of these electrodes come from pseudocapacitive or capacitive phenomena. With this information a well-based synthetic strategy could be developed in order to achieve the highest electrochemical specific capacitance possible. Also the cyclic stability would be required to validate the specific capacitances of the best proposed samples. A more detailed physico-chemical characterisation before and after cycling would be essential to better understand the pseudocapacitive behaviour.

8. References

1. Wang, G., Zhang, L., Zhang, J., A review of electrode materials for electrochemical supercapacitors. *Chem. Soc. Rev.* **2012,** *41*, 797-828.
2. Tateishi, H., Koinuma, M., Miyamoto, S., Kamei, Y., Hatakeyama, K., Ogata, C., Taniguchi, T., Funatsu, A., Matsumoto, Y., Effect of the Electrochemical Oxidation/Reduction Cycle on the Electrochemical Capacitance of Graphite Oxide. *Carbon* **2014**.
3. Nasibi, M., Golozar, A. M., Rashed, G. , Nanoporous carbon black particles as an electrode material for electrochemical double layer capacitors. *Mater. Lett.* **2013,** *91*, 323-325.
4. Lia, Y., van Zijllb, M., Chiangb, S., Pana, N., KOH modified graphene nanosheets for supercapacitor electrodes. *J. Power Sourc.* **2011,** *196*, 6003-6006.
5. Singsanga, W., Panapoya, M., Ksapabutra, B., Facile one-pot synthesis of freestanding carbon nanotubes on cellulose-derived carbon films for supercapacitor applications: effect of the synthesis temperature. *Energy Procedia* **2014,** *56*, 439 – 447.
6. Luo, Y., Zhang, H., Guo, D., Ma, J., Li, Q., Chen, L., Wang, T., Porous NiCo2O4-reduced graphene oxide (rGO) composite with superior capacitance retention for supercapacitors. *Electrochim. Acta* **2014,** *132*, 332-337.
7. Yang, S., Cheng, K., Huang, J., Ye, K., Xu, Y, Cao, D., Zhang, X., Wang, G., High-capacitance MnO2 nanoflakes on preformed C/TiO2 shell/core nanowire arrays for electrochemical energy storage. *Electrochim. Acta* **2014,** *120*, 416-422.
8. Three-Dimensional Self-Supported Metal Oxides for Advanced Energy Storage. *Adv. Mater.* **2014,** *26*, 3368-3397.
9. PANIĆ, V. V., DEKANSKI, A. B., NIKOLIĆ, B. Ž., Tailoring the supercapacitive performances of noble metal oxides, porous carbons and their composites. *J. Serb. Chem. Soc.* **2013,** *78* (12), 2141-2164.
10. Vidhyadharan, B., Zain, N. K. M., Misnon, I. I., Aziz, R. A., Ismail, J., Yusoff, M. M., Jose, R. , High performance supercapacitor electrodes from electrospun nickel oxide nanowires. *J. All. Compounds* **2014,** *610*, 143-150.
11. Wang, Y., Gai, S., Li, C., He, F., Zhang, M., Yan, Y., Yang, P., Controlled synthesis and enhanced supercapacitor performance of uniform pompon-like β-Ni(OH)2 hollow microspheres. *Electrochim. Acta* **2013,** *90*, 673-681.
12. Yang, J., Lan, T., Liu, J., Song, Y., Wei, M., Supercapacitor electrode of hollow spherical V2O5 with a high pseudocapacitance in aqueous solution. *Electrochim. Acta* **2013,** *105*, 489-495.
13. Silva, R. P., Eugénio, S., Silva, T. M., Carmezim, M. J., Montemor, M. F., Fabrication of Three-Dimensional Dendritic Ni−Co Films By Electrodeposition on Stainless Steel Substrates. *J. Phys. Chem. C* **2012,** *116*, 22425-22431.
14. Zhou, H., Chen, H., Luo, S., Lu, G., Wei, W., Kuang, Y., The effect of the polyaniline morphology on the performance of polyaniline supercapacitors. *J. Solid. State Electrochem.* **2005,** *9*, 574-580.
15. Dubal, D. P., Patil, S. V., Kim, W. B., Lokhande, C. D., Supercapacitors based on electrochemically deposited polypyrrole nanobricks. *Mater. Lett.* **2011,** *65*, 2628–2631.
16. Pandeya, G. P., Rastogi, A. C., Synthesis and characterization of pulsed polymerized poly(3,4-ethylenedioxythiophene) electrodes for high-performance electrochemical capacitors. *Electrochim. Acta* **2013,** *87*, 158-168.
17. Dubal, D. P., Patil, S. V., Gundb, G. S., Lokhande, C. D., Polyaniline–polypyrrole nanograined composite via electrostatic adsorption for high performance electrochemical supercapacitors. *J. All. Compounds* **2013,** *552*, 240-247.
18. Fua, M., Geb, C., Houc, Z., Zeng, F., Kuang, Y., Cao, J., Hec, B., Graphene/vanadium oxide nanotubes composite as electrode material for electrochemical capacitors. *Physica B* **2013,** *421*, 77-82.
19. Jiang, X., Setodoi, S., Fukumoto, S., Imae, I., Komaguchi, K., Yano, J., Mizota, H., Harima, Y., An easy one-step electrosynthesis of graphene/polyaniline composites and electrochemical capacitor. *Carbon* **2014,** *67*, 662-672.

20. Wang, Q., Jiao, L., Duc, H., Wang, Y., Yuanc, H., Fe3O4 nanoparticles grown on graphene as advanced electrode materials for supercapacitors. *J. Power Sourc.* **2014,** *245*, 101-106.
21. Jurewicz, K., Delpeux, S., Bertagna, V., Béguin, F., Frackowiak, E., Supercapacitors from nanotubes/polypyrrole composites. *Chem. Phys. Lett.* **2001,** *347*, 36-40.
22. Lia, H., Wang, J., Chub, Q., Wang, Z., Zhanga, F., Wang, S., Theoretical and experimental specific capacitance of polyaniline in sulfuric acid. *J. Power Sourc.* **2009,** *190*, 578-586.
23. Prasad, K. R., Munichandraiah, N., Fabrication and evaluation of 450 F electrochemical redox supercapacitors using inexpensive and high-performance, polyaniline coated, stainless-steel electrodes. *J. Power Sourc.* **2002,** *112*, 443-451.
24. Bavio, M. A., Acosta, G. G., Kessler, T., Polyaniline and polyaniline-carbon black nanostructures as electrochemical capacitor electrode materials. *Int. J. Hydrogen. Energ.* **2014,** *39*, 8582-8589.
25. Li, D., Huang, J., Kaner, R. B., Polyaniline nanofibers: a unique polymer nanostructure for versatile applications. *Acc. Chem. Res.* **2009,** *42* (1), 135-145.
26. Ansari, J., Keivani, M. B., Polyaniline Conducting Electroactive Polymers: Thermal and Environmental Stability Studies. *E-J. Chem.* **2006,** *3* (4), 202-217.
27. Bhadra, S., Khastgir, D., Singha, N. K., Lee, J. H., Progress in preparation, processing and applications of polyaniline. *Prog. Polym. Sci.* **2009,** *34*, 783-810.
28. Conway, B. E., *Electrochemical Supercapacitors - Scientific Fundamentals and Technological Applications*. Kluwer Academic: New York, 1999.
29. Sapurina, I., Stejskal, J., The mechanism of the oxidative polymerization of aniline and the formation of supramolecular polyaniline structures. *Polym. Int.* **2008,** *57*, 1295-1325.
30. Pahovnik, D., Žagar, E., Vohlidal, J., Žigon, M., Effect of cations on polyaniline morphology. *Chem. Pap.* **2013,** *67* (8), 946-951.
31. Peng., X.-Y., Luan, F., Liu, X-X., Diamond, D., Lau, K-T., pH-controlled morphological structure of polyaniline during electrochemical deposition. *Electrochim. Acta* **2009,** *54*, 6172-6177.
32. Li, W., Wang, H-L., Oligomer-Assisted Synthesis of Chiral Polyaniline Nanofibers. *J. Am. Chem. Soc.* **2004,** *126*, 2278-2279.
33. Karami, H., Asadi, M. G., Mansoori, M., Pulse electropolymerization and the characterization of polyaniline nanofibers. *Electrochim. Acta* **2012,** *61*, 154-164.
34. Valentová, H., Prokeš, J., Nebdal, J., Stejskal, J., Effect of compression pressure on mechanical and electrical properties of polyaniline pellets. *Chem. Pap.* **2013,** *67* (8), 1109-1112.
35. Ćirić-Marjanović, G., Pašti, I., Gavrilov, N., Janošević, A., Mentus, S. , Carbonised polyaniline and polypyrrole: towards advanced nitrogen-containing carbon materials. *Chem. Pap.* **2013,** *67* (8), 781-813.
36. Libert, J., Cornil, J., dos Santos, D. A., Brédas, J. L., Form neutral oligoanilines to polyanilines: A theoretical investigation of the chain-length dependence of the electronic and optical properties. *Phys. Rev. B* **1997,** *56* (14), 8638-8650.
37. Zhang, H., Lu, J., Wang, X., Li, J., Wang, F., From amorphous to crystalline: Practical way to improve electrical conductivity of water-borne conducting polyaniline. *Polymer* **2011,** *52*, 3059-3064.
38. Pfitzner, A., Dankesreiter, S., Eisenhofer, A., Cherevatskaya, Heterogeneous Semiconductor Photocatalysis. In *Chemical Photocatalysis*, König, B., Ed. de Gruyter: Göttingen, 2013; pp 211-245.
39. Di Paola, A., Bellardita, M., Palmisano, L., Brookite, the Least Known TiO2 Photocatalyst. *Catalysts* **2013,** *3*, 36-73.
40. Goldstein, J. I., Newbury, D. E., Echlin, P., Joy, D. C., Romig Jr., A. D., Lyman, C. E., Fiori, C., Lifshin, E., *Scanning Electron Microscopy and X-Ray Microanalysis - A Text for Biologists, Materials Scientists, and Geologists*. 2nd Edition ed.; Plenum Press: New York, 1992.
41. Achaw, O.-W., *A Study of the Porosity of Activated Carbons Using the Scanning Electron Microscope*. InTech: Croatia, 2012.

42. *Handbook of Raman Spectroscopy - From the Research Laboratory to the Process Line*. Marcel Dekker, Inc.: New York, 2001.
43. Dietzek, B., Cialla, D., Schmitt, M., Popp, J., Introduction to the Fundamentals of Raman Spectroscopy. In *Raman Microscopy - Developments and Applications*, 1st Edition ed.; Turrell, G., Ed. Elsevier: London, 1996; pp 21-42.
44. de Faria, D. L. A., Silva, S. V., de Oliveira, M. T. , Raman Microspectroscopy of Some Iron Oxides and Oxyhydroxides. *J. Raman Spectrosc.* **1997,** *28*, 873-878.
45. Popović, L., de Waal, D., J. C. A., Boeyens, Correlation between Raman wavenumbers and P—O bond lengths in crystalline inorganic phosphates. *J. Raman Spectrosc.* **2005,** *36*, 2-11.
46. Ćirić-Marjanović, G., Trchová, M., Stejskal, J. , The chemical oxidative polymerization of aniline in water: Raman spectroscopy. *J. Raman Spectrosc.* **2008,** *39*, 1375-1387.
47. Yang, J. J., Martens, W. N., Frost, R. L., Transition of chromium oxyhydroxide nanomaterials to chromium oxide: a hot-stage Raman spectroscopic study. *J. Raman Spectrosc.* **2010,** *42*, 1142–1146.
48. W. L. A., A., C. L. L., Chai, *Purification of Laboratory Chemicals*. Butterworth-Heinemann: USA, 2009.
49. Horiba Horiba LabRAM HR Evolution http://www.horiba.com/fileadmin/uploads/Scientific/Documents/Raman/LabRAM_HR_Evolution.pdf.
50. Bobacka, J., Lewenstam, A., Ivaska, A., Electrochemical impedance spectroscopy of oxidized poly(3,4-ethylenedioxythiophene) film electrodes in aqueous solutions. *J. Electroanal. Chem.* **2000,** *489*, 17-27.
51. Miller Jr., P. H., The Electrical Conductivity of Zinc Oxide. *Phys. Rev.* **1941,** *60*, 890.
52. Bhide, V. G., Dani, R. H., Electrical conductivity in oxides of manganese and related compounds. *Physica* **1961,** *27* (9), 821-826.
53. Conway, B. E., Impedance Behavior of Electrochemical Supercapacitors and Porous Electrodes. In *Impedance Spectroscopy - Theory, Experiment, and Applications*, 2nd Edition ed.; Barsoukov, E., Macdonald, J. R., Ed. John Wiley & Sons: New Jersey, 2005; pp 469-496.